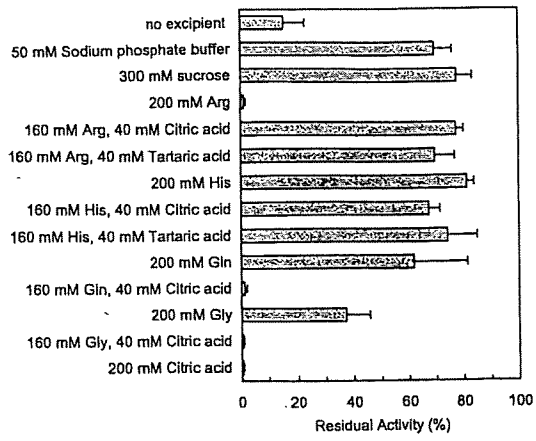


Fig. 9. Effect of Amino Acid and Organic Acid Combinations on the Activity of Freeze-Dried Lactate Dehydrogenase (50 $\mu$g/ml, Average±S.D., $n$=3)

nine freeze-dried with inorganic acids (*e.g.*, HCl, $H_3PO_4$).[13] A carboxyl group band at 1725 $cm^{-1}$ appeared when the citric acid ratio was increased. Diffuse-reflection near-infrared spectra obtained non-destructively at the bottom of the glass vials also indicated the altered local environment of the functional groups. A large amino band of L-arginine (6505 $cm^{-1}$, N–H stretching 1st overtone) disappeared in the presence of lower molar concentration ratio of citric acid in the initial solution (140 mM L-arginine, 60 mM citric acid). Increasing the citric acid ratio also reduced the large absorption band at 4920 $cm^{-1}$, and concomitantly induced band at 5030 $cm^{-1}$ in the co-lyophilized solids. Assignment of these bands remains to be elucidated. The results strongly suggested hydrogen-bonding and/or electrostatic interactions between L-arginine and citric acid in the lyophilized solids.

**Effect of Excipients on Inactivation of Freeze-Dried LDH** Freeze-drying of LDH in the absence of the stabilizing excipients resulted in significant reduction of the activity (approximately 15% of the initial solution) (Fig. 9). Higher enzyme activity was retained in freeze-drying at a higher phosphate buffer concentration (50 mM). Some amino acid and organic acid combinations that provide neutral to weakly acidic initial solution (pH 5—8) and amorphous dried solids also retained the enzyme activity. The enzyme lost most of the activity in freeze-drying from extreme pH solutions (*e.g.*, 200 mM L-arginine, pH 10.6). Addition of citric acid or L-tartaric acid slightly reduced the effect of L-histidine to retain the activity of LDH during freeze-drying. Crystallization of glycine in the single-solute frozen solution, and concomitant loss of the protecting effect, should explain the lower remaining enzyme activity.[1,2,22]

## Discussion

The freeze-drying of aqueous solutions containing some basic or neutral amino acid (*e.g.*, L-arginine, L-histidine) and hydroxy di- or tricarboxylic acid (*e.g.*, citric acid, L-tartaric acid) combinations resulted in the glass-state amorphous solid cakes that protect proteins from dehydration stresses. Some of the solids showed glass transition temperatures comparable to those of disaccharides (*e.g.*, sucrose, trehalose).[4] The data and recent literature on the properties of related substances in different physical states (*e.g.*, complex crystals, ionic liquids) strongly suggested contribution of the multiple functional groups of the consisting molecules to form the interaction (*e.g.*, electrostatic, hydrogen-bonding) networks required for the glass-state amorphous solids.[23—25] Multiple amino, carboxyl, and hydroxyl groups in the solute molecules raise transition temperatures of the mixture frozen solutions ($T_g'$) and the freeze-dried solids ($T_g$).[15] The ammonium carbohydrate ion pairs form multiple hydrogen-bondings in some non-polar solvents.[23,24] Differently protonated carboxyl and carboxylate groups also form an intermolecular hydrogen-bonding network.[25]

The amino acids and organic acids containing plural amino or carboxyl groups should have large chance to form the interactions with multiple counterpart molecules. The contribution of the multiple functional groups should explain the high transition temperatures ($T_g'$, $T_g$) of the L-arginine and citric acid combination. L-Arginine also forms stable amorphous freeze-dried solids with multivalent inorganic acids (*e.g.*, $H_3PO_4$).[11,13] Frozen sodium citrate and tartrate buffer solutions exhibit the highest $T_g'$ at certain sodium concentration ratios.[17] Supramolecular interactions (*e.g.*, peptide-like periodic interactions) reported in some complex crystals of amino acid and dicarboxylic acid (*e.g.*, L-arginine and adipic acid, X-ray analysis)[26] should support the possible multi-molecular interaction network in the less-ordered amorphous phase.

Hydroxyl groups in the citric acid, L-tartaric acid, and DL-malic acid should introduce additional hydrogen bonding to the amorphous phase. The number of hydroxyl groups in the component, and the accompanying change in the molecular interactions are major factors in determining the glass transition temperature of some ionic liquids composed of an amino acid and a 1-allylimidazolium cation.[27] The intense interactions and resulting reduction of the molecular mobility may prevent the crystallization of amino acids (*e.g.*, glycine, glutamine) at concentration ratios much lower than those of "inert" nonionic solutes (*e.g.*, sucrose) or inorganic salts (*e.g.*, NaCl).[17,30—32]

The high glass transition temperature amorphous solids formed by combinations of popular excipients would be a practical alternative to disaccharides in the design of freeze-dried protein formulations. The excipient combinations would satisfy the two major protein-stabilizing mechanisms postulated on saccharides, namely substitution of the surrounding water molecules by hydrogen-bonding and reduction of the chemical reaction by embedding in the glass-state solids.[6—8] Additional effects of some amino acids (*e.g.*, reduced aggregation in aqueous solution by L-arginine) preferable in protein formulations are also anticipated.[9] The limited crystallinity and low volatility of the amino acid and organic acid should reduce the risk of pH change and the resulting protein inactivation in the freeze-drying process reported in some buffer systems.[28]

Various proteins degrade during the freeze-drying process and subsequent storage through several chemical and physical mechanisms.[3,29] The low concentration LDH solution is often used as a model system for studying the effect of co-solutes in the freeze-thawing and freeze-drying processes because of its apparent tendency to lose its activity due to irreversible subunit dissociation and conformation change.[30] The ability of excipient combinations to retain the enzyme

activity in the freeze-drying process should indicate the stabilization of the quarterly structure against freeze-concentration and dehydration stress. Different molecular mobility, local pH, water content, and crystallinity of the excipients may affect the chemical degradation rate of the freeze-dried enzyme in the subsequent storage. The freeze-dried basic amino acid and organic acid combination solids should provide the embedded proteins with unique local environments that are significantly different from those of the nonionic excipients (*e.g.*, saccharides). The structural and chemical stability of proteins in these solids during the freeze-drying process and storage is an intriguing topic that needs further study through various model protein and stress systems.

**References**


1) Nail S. L., Jiang S., Chongprasert S., Knopp S. A., *Pharm. Biotechnol.*, **14**, 281—360 (2002).
2) Tang X., Pikal M. J., *Pharm. Res.*, **21**, 191—200 (2004).
3) Carpenter J. F., Arakawa T., Crowe J. H., *Dev. Biol. Stand.*, **74**, 225—238 (1992).
4) Franks F., *Dev. Biol. Stand.*, **74**, 9—18 (1992).
5) Lee J. C., Timasheff S. N., *J. Biol. Chem.*, **256**, 7139—7201 (1981).
6) Chang B. S., Randall C., *Cryobiology*, **29**, 632—656 (1992).
7) Arakawa T., Timasheff S. N., *Arch. Biochem. Biophys.*, **224**, 169—177 (1983).
8) Sane S. U., Wong R., Hsu C. C., *J. Pharm. Sci.*, **93**, 1005—1018 (2004).
9) Tsumoto K., Umetsu M., Kumagai I., Ejima D., Philo J. S., Arakawa T., *Biotechnol. Prog.*, **20**, 1301—1308 (2004).
10) Osterberg T., Fatouros A., Mikaelsson M., *Pharm. Res.*, **14**, 892—898 (1997).
11) Mattern M., Winter G., Kohnert U., Lee G., *Pharm. Dev. Technol.*, **4**, 199—208 (1999).
12) Osterberg T., Wadsten T., *Eur. J. Pharm. Sci.*, **8**, 301—308 (1999).
13) Izutsu K., Fujimaki Y., Kuwabara A., Aoyagi N., *Int. J. Pharm.*, **301**, 161—169 (2005).
14) Li J., Chatterjee K., Medek A., Shalaev E., Zografi G., *J. Pharm. Sci.*, **93**, 697—712 (2004).
15) Kadoya S., Izutsu K., Yonemochi E., Terada K., Yomota C., Kawanishi T., *Chem. Pharm. Bull.*, **56**, 821—826 (2008).
16) Akers M. J., Milton N., Byrn S. R., Nail S. L., *Pharm. Res.*, **12**, 1457—1461 (1995).
17) Shalaev E. Y., Johnson-Elton T. D., Chang L., Pikal M. J., *Pharm. Res.*, **19**, 195—201 (2002).
18) Chongprasert S., Knopp S. A., Nail S. L., *J. Pharm. Sci.*, **90**, 1720—1728 (2001).
19) Lu Q., Zografi G., *J. Pharm. Sci.*, **86**, 1374—1378 (1997).
20) Shamblin S. L., Taylor L. S., Zografi G., *J. Pharm. Sci.*, **87**, 694—701 (1998).
21) Yonemochi E., Inoue Y., Buckton G., Moffat A., Oguchi T., Yamamoto K., *Pharm. Res.*, **16**, 835—840 (1999).
22) Anchordoquy T. J., Carpenter J. F., *Arch. Biochem. Biophys.*, **332**, 231—238 (1996).
23) Sada K., Tani T., Shinkai S., *Synlett*, **2006**, 2364—2374 (2006).
24) Yerger E. A., Barrow G. M., *J. Am. Chem. Soc.*, **77**, 6206—6207 (1955).
25) Kobayashi N., Naito T., Inabe T., *Bull. Chem. Soc. Jpn.*, **76**, 1351—1362 (2003).
26) Roy S., Singh D. D., Vijayan M., *Acta Crystallogr. B*, **61**, 89—95 (2005).
27) Fukumoto K., Yoshizawa M., Ohno H., *J. Am. Chem. Soc.*, **127**, 2398—2399 (2005).
28) Li J., Guo Y., Zografi G., *Pharm. Res.*, **19**, 20—26 (2002).
29) Manning M. C., Patel K., Borchardt R. T., *Pharm. Res.*, **6**, 903—918 (1989).
30) Seguro K., Tamiya T., Tsuchiya T., Matsumoto J. J., *Cryobiology*, **27**, 70—79 (1990).

# Feasibility of $^{19}$F-NMR for Assessing the Molecular Mobility of Flufenamic Acid in Solid Dispersions

Yukio Aso,* Sumie Yoshioka, Tamaki Miyazaki, and Toru Kawanishi

*National Institute of Health Sciences; 1–18–1 Kamiyoga, Setagaya, Tokyo 158–8501, Japan.*
Received September 9, 2008; accepted October 22, 2008; published online October 23, 2008

**The purpose of the present study was to clarify the feasibility of $^{19}$F-NMR for assessing the molecular mobility of flufenamic acid (FLF) in solid dispersions. Amorphous solid dispersions of FLF containing poly(vinylpyrrolidone) (PVP) or hydroxypropylmethylcellulose (HPMC) were prepared by melting and rapid cooling. Spin–lattice relaxation times ($T_1$ and $T_{1\rho}$) of FLF fluorine atoms in the solid dispersions were determined at various temperatures (−20 to 150 °C). Correlation time ($\tau_c$), which is a measure of rotational molecular mobility, was calculated from the observed $T_1$ or $T_{1\rho}$ value and that of the $T_1$ or $T_{1\rho}$ minimum, assuming that the relaxation mechanism of spin–lattice relaxation of FLF fluorine atoms does not change with temperature. The $\tau_c$ value for solid dispersions containing 20% PVP was 2—3 times longer than that for solid dispersions containing 20% HPMC at 50 °C, indicating that the molecular mobility of FLF in solid dispersions containing 20% PVP was lower than that in solid dispersions containing 20% HPMC. The amount of amorphous FLF remaining in the solid dispersions stored at 60 °C was successfully estimated by analyzing the solid echo signals of FLF fluorine atoms, and it was possible to follow the overall crystallization of amorphous FLF in the solid dispersions. The solid dispersion containing 20% PVP was more stable than that containing 20% HPMC. The difference in stability between solid dispersions containing PVP and HPMC is considered due to the difference in molecular mobility as determined by $\tau_c$. The molecular mobility determined by $^{19}$F-NMR seems to be a useful measure for assessing the stability of drugs containing fluorine atoms in amorphous solid dispersions.**

Key words $^{19}$F-NMR; molecular mobility; stability; crystallization; solid dispersion

Amorphous solid dispersions are used for improving the dissolution rate and solubility of poorly soluble drugs. However, drugs in amorphous form are generally less stable than crystalline drugs because of their higher energy state and higher molecular mobility. It is well known that polymeric excipients can reduce the crystallization rate of many amorphous drugs.[1—12] This stabilization by poly(vinylpyrrolidone) (PVP) is partly attributable to its ability to decrease molecular mobility, as indicated by increases in the glass transition temperature ($T_g$).[9] Therefore, it is of great interest to estimate the molecular mobility of drugs in solid dispersions. Although $^{13}$C-NMR relaxation measurements are useful for assessing the molecular mobility of drugs in solid dispersions,[13] the low sensitivity of $^{13}$C because of its low natural abundance is a drawback of $^{13}$C-NMR. In contrast to $^{13}$C, $^{19}$F has very favorable sensitivity in NMR experiments, since it is present in 100% natural abundance, is second only to the proton in its resonance frequency (except $^3$H) and has a spin quantum number of 1/2. The receptivity for $^{19}$F is 83% of that for $^1$H and 4700 times of that for $^{13}$C.[14] Many drugs containing fluorine atoms are listed in The Japanese Pharmacopoeia. In contrast, almost all pharmaceutical excipients do not contain fluorine atoms. $^{19}$F-NMR may therefore have an advantage over $^{13}$C-NMR or $^1$H-NMR for selectivity and sensitivity when assessing the molecular mobility of drugs containing fluorine atoms in pharmaceutical dosage forms such as solid dispersions.

The orientations and molecular mobility of flufenamic acid (FLF)[15] and $^{19}$F-labeled $\alpha$-tocopherol[16] in a lipid bilayer were studied using $^{19}$F-NMR. Structures and molecular mobility of $^{19}$F-labeled peptides and proteins in biological membranes were also investigated.[17—20] To the authors' knowledge, application of $^{19}$F-NMR to studies of drug molecular mobility in solid dispersions has not been reported. This paper describes the feasibility of $^{19}$F-NMR for assessing the molecular mobility of FLF in PVP or hydroxypropylmethylcellulose (HPMC) solid dispersions, and discusses the effect of polymer excipients on the crystallization tendency of FLF in solid dispersions in terms of differences in molecular mobility.

## Experimental

**Materials** FLF (Fig. 1) was purchased from Wako Pure Chemical Industry (Osaka), and PVP and HPMC were from Sigma (St. Louis, MO, U.S.A.). FLF solid dispersions with PVP or HPMC were prepared by melting and cooling of mixtures of FLF with PVP or HPMC. The solid dispersions obtained were confirmed to be amorphous from microscopic observation under polarized light.

**Nuclear Magnetic Relaxation Measurements** $^{19}$F-NMR measurements were carried out using a model JNM-MU25 pulsed NMR spectrometer (JEOL DATUM, Tokyo) operating at a resonance frequency of 25 MHz. Time profiles of spin–spin relaxation of the $^{19}$F atoms of FLF were measured using the "solid echo" pulse sequence to overcome the dead time of the instrument. Spin–lattice relaxation time in the laboratory frame ($T_1$) was measured using the inversion recovery pulse sequence. Spin–lattice relaxation time in the rotating flame ($T_{1\rho}$) was measured at spin locking intensity of 10 G.

**DSC Measurements** $T_g$ of FLF-PVP and FLF-HPMC solid dispersions was measured by DSC using a model 2920 differential scanning calorimeter and a refrigerator cooling system (TA Instruments, Newcastle, DE, U.S.A.). Approximately 5 mg of each solid dispersions was put into an aluminum sample pan and then sealed hermetically. $T_g$ was measured at a heating rate of 20 °C/min. Temperature calibration of the instrument was carried out using indium.

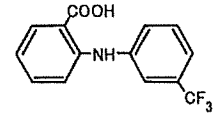


Fig. 1. Structure of FLF

* To whom correspondence should be addressed. e-mail: aso@nihs.go.jp

## Results and Discussion

**Molecular Mobility of FLF as Measured by $^{19}$F-NMR Spin–Lattice Relaxation Time** $T_1$ and $T_{1\rho}$ of fluorine atoms of FLF in PVP and HPMC solid dispersions were measured using a pulsed NMR spectrometer in the temperature range from −20 to 150 °C. $T_1$ is sensitive to the molecular motion on the time scale of the resonance frequency (MHz order). On the other hand, $T_{1\rho}$ is sensitive to the molecular motion with a frequency equivalent to the intensity of spin locking field (typically mid kHz order).[21] The temperature dependence of $T_1$ and $T_{1\rho}$ exhibits minimum at a specific temperature at which the molecules of interest have molecular motion with MHz time scale or mid kHz time scale predominantly. The resonance frequency of 25 MHz, lower than that of a conventional high resolution NMR spectrometer, was used to observe $T_1$ minimum in the temperature rage studied. Figure 2 shows the temperature dependence of $T_1$ and $T_{1\rho}$ of FLF fluorine atoms in PVP and HPMC solid dispersions. For FLF–PVP solid dispersions (7 : 3), the minimum of $T_1$ or $T_{1\rho}$ was observed at about 90 °C and 60 °C, respectively (Fig. 2A). When the PVP content decreased to 20% (w/w), $T_1$ and $T_{1\rho}$ of FLF at temperatures above 70 °C could not be determined due to rapid crystallization. Similar temperature dependence of $T_1$ or $T_{1\rho}$ was observed for the FLF–HPMC solid dispersions (Fig. 2B). The temperature difference between $T_1$ and $T_{1\rho}$ minimum is considered to be due to the difference in the time scale of molecular motion reflected on $T_1$ (MHz order) and $T_{1\rho}$ (mid kHz order). Since the molecular motion on MHz time scale becomes predominant at higher temperature than molecular motion on mid kHz time scale, $T_1$ minimum is observed at higher temperature than $T_{1\rho}$ minimum.

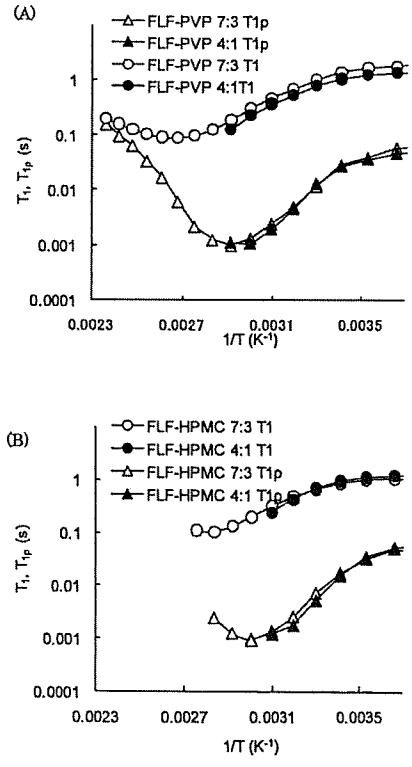


Fig. 2. Temperature Dependence of $T_1$ and $T_{1\rho}$ of FLF Fluorine Atoms in PVP (A) and HPMC (B) Solid Dispersions

We made following assumptions in order to estimate the molecular mobility of FLF from $T_1$ and $T_{1\rho}$ of FLF fluorine atoms: first, we assumed that FLF fluorine atoms in the solid dispersions relaxes mainly *via* dipolar interaction, and that the contribution of the spin–rotation interaction mechanism[21] is negligible. While relaxation *via* the spin–rotation interaction mechanism has been reported for liquid sample,[22–24] complete domination of dipolar interactions has been reported for fluorine atoms for polycrystalline van der Waals molecular solid.[25] We also made an assumption that the contribution of the cross-relaxation between fluorine and proton atoms can be considered small. It is known that relaxation is not intrinsically single-exponential when cross-relaxation between fluorine and proton atoms takes place.[14] However, we assumed small contribution of the cross-relaxation, because the relaxation of FLF fluorine atoms in the solid dispersions was exponential within experimental uncertainty. In studies of molecular motions, a large number of models describing molecular motions have been proposed for calculation of the spectrum density function.[26] We used a simple model that the molecular motion reflected on $T_1$ or $T_{1\rho}$ is represented by single correlation time for the purpose of comparing the mobility of FLF in the PVP and HPMC solid dispersions. According to the above assumptions, $T_1$ and $T_{1\rho}$ are described by Eqs. 1 and 2.[21]

$$\frac{1}{T_1} = \frac{6}{20}\frac{\gamma^4\hbar^2}{r^6}\left\{\frac{\tau_c}{1+\omega_0^2\tau_c^2} + \frac{4\tau_c}{1+4\omega_0^2\tau_c^2}\right\} \quad (1)$$

$$\frac{1}{T_{1\rho}} = \frac{3}{20}\frac{\gamma^4\hbar^2}{r^6}\left\{\frac{3\tau_c}{1+4\omega_1^2\tau_c^2} + \frac{5\tau_c}{1+\omega_0^2\tau_c^2} + \frac{2\tau_c}{1+4\omega_0^2\tau_c^2}\right\} \quad (2)$$

where $\tau_c$ is the correlation time that characterizes molecular reorientations, and $\omega_0$ and $\omega_1$ are the resonance frequencies of fluorine atoms in the static magnetic field and spin locking field, respectively. $\gamma$, $r$ and $\hbar$ are the gyromagnetic ratio of fluorine, the distance of neighboring fluorine atoms, and the Plank constant divided by $2\pi$, respectively. Equations 1 and 2 infer that $T_1$ and $T_{1\rho}$ become minimal when $\omega_0\tau_c$ is approximately 0.62[27] and $\omega_1\tau_c$ is approximately 0.52,[21] respectively. When the minimum of $T_1$ or $T_{1\rho}$ is observed, we can calculate the unknown value, $r$, in Eqs. 1 and 2. If $r$ is known, the $\tau_c$ value can be calculated from the observed $T_1$ or $T_{1\rho}$ value, assuming that $r$ does not change with temperature.

The values of $r$ calculated from the $T_1$ and $T_{1\rho}$ minimum observed for the FLF–PVP solid dispersion (7 : 3) were 2.3 and 2.4 Å, respectively, and similar $r$ values were obtained for the FLF–HPMC solid dispersion (7 : 3). These values are comparable to the reported value (2.174 Å) for 3-(trifluoromethyl)phenanthrene,[25] indicating that dipole interaction between neighboring fluorine atoms can be considered the predominant relaxation mechanism of FLF fluorine atoms in the solid dispersions. The difference between the $r$ values obtained in this work and the reported value suggests that the possibility of the spin–rotation interaction mechanism and/or dipole interaction between fluorine and proton atoms cannot be excluded as a relaxation mechanism of FLF fluorine atoms.

Figure 3 shows the temperature dependence of $\tau_c$ calculated from $T_1$ and $T_{1\rho}$ for FLF fluorine atoms in the solid dis-

persions. The $\tau_c$ of FLF fluorine atoms in PVP solid dispersions calculated from $T_{1\rho}$ was 8.2 $\mu$s at 50 °C, which was about 3 times larger than that in HPMC solid dispersions (2.6 $\mu$s), indicating that the molecular mobility of FLF was lowered more strongly by PVP than by HPMC.

The $\tau_c$ values calculated using $T_1$ values differ from those calculated from $T_{1\rho}$ values. The slope of temperature dependence of $\tau_c$ changed around $T_g$. These findings suggest that the assumption that the molecular motion reflected on $T_1$ and $T_{1\rho}$ is represented by a single $\tau_c$ may be too simple to describe the molecular motion of FLF in the solid dispersions at temperatures studied, and that two or more molecular motions, such as rotation of trifluoromethyl group and motions with larger scales than rotation of trifluoromethyl group, may be reflected on $T_1$ and $T_{1\rho}$. Further studies including $^1$H-NMR relaxation measurement and dielectric relaxation measurements will be needed to identify the detailed molecular motion of FLF in the solid dispersions.

**Correlation between Crystallization Tendency and Molecular Mobility of FLF in Solid Dispersions** Crystallization proceeds *via* formation of crystal nuclei and crystal growth. As a measure of the crystallization tendency of amorphous FLF in solid dispersions, the overall crystallization rate of amorphous FLF in the solid dispersions was estimated from the time profiles amorphous FLF remaining in the solid dispersions instead of measuring the nucleation rate and growth rate. Amorphous FLF remaining in the solid dispersions was estimated by analyzing solid echo signals of FLF fluorine atoms. Figure 4 shows the solid echo signal of fluorine atoms of FLF in solid dispersions containing 20% (w/w) PVP and that of fluorine atoms of crystalline FLF. The signal for the solid dispersions was describable by the Lorentzian relaxation equation (Eq. 3), and its relaxation time ($T_{2L}$) was approximately 140 $\mu$s. Crystalline FLF exhibited Gaussian relaxation signals (Eq. 4), and its relaxation time ($T_{2G}$) was approximately 30 $\mu$s. These results indicate that amorphous FLF in solid dispersions is considered to exhibit Lorentzian relaxation signals.

$$I=I_0 \exp(-t/T_{2L}) \tag{3}$$

$$I=I_0 \exp\{-t^2/(2T_{2G}^2) \tag{4}$$

where $I_0$ and $I$ represent the signal intensities at time 0 and $t$, respectively. Figure 5 shows solid echo signals for the fluorine atoms of FLF in the solid dispersions stored at 60 °C. Samples stored at 60 °C exhibited biphasic decay signals, and signals were describable by summation of the Gaussian (solid line) and Lorentzian (dashed line) equations (Eq. 5).

$$I=I_0\{P_L \exp(-t/T_{2L})+P_G \exp(-t^2/2T_{2G}^2)\} \tag{5}$$

where $P_L$ and $P_G$ are the ratio of fluorine atoms exhibiting Lorentzian and Gaussian relaxation process, respectively, and $P_L+P_G=1$. Assuming that the $T_{2L}$ and $T_{2G}$ values are 140 and 30 $\mu$s, respectively, $P_L$ values of FLF in the solid dispersions were estimated by curve fitting. $P_L$ values of the solid dispersions decreased with increasing storage time, indicating that crystallization of amorphous FLF in solid dispersions takes place during storage at 60 °C. To certify the reliability of the $P_L$ values obtained by $^{19}$F-NMR measurements, change in the heat capacity at $T_g$ ($\Delta C_p(T_g)$) was determined for the solid dispersions stored at 60 °C for various periods as a measure of amorphous FLF remaining, and was compared with the value of $P_L$. As shown in Fig. 6, the $P_L$ value was proportional to the $\Delta C_p(T_g)$ value, and was considered to be a useful measure of amorphous FLF remaining in the solid dispersions.

Figure 7 shows the time profiles of the $P_L$ values for FLF solid dispersions containing 20% (w/w) PVP or HPMC at 60 °C. The decrease in the ratio of Lorentzian fluorine atoms was faster for HPMC solid dispersions than for PVP solid dispersions, indicating that the overall crystallization rate of FLF in HPMC solid dispersions is larger than that in PVP solid dispersions. The overall crystallization rate depends on both molecular mobility (the rate of diffusion across the interface between crystalline and amorphous phase) and ther-

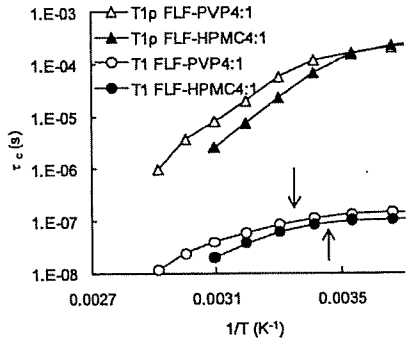


Fig. 3. Temperature Dependence of $\tau_c$ of FLF Fluorine Atoms in PVP and HPMC Solid Dispersions

Arrows in the figure represent $T_g$.

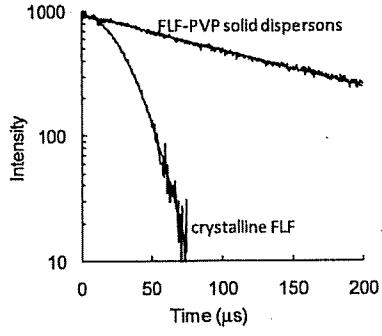


Fig. 4. Typical Solid Echo Signal of Fluorine Atoms of FLF in the Freshly Prepared Solid Dispersion Containing 20% (w/w) PVP and That of Fluorine Atoms of Crystalline FLF

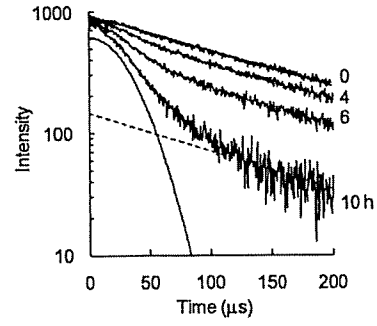


Fig. 5. Typical Solid Echo Signals of Fluorine Atoms of FLF in the Solid Dispersions Containing 20% (w/w) PVP Stored at 60 °C

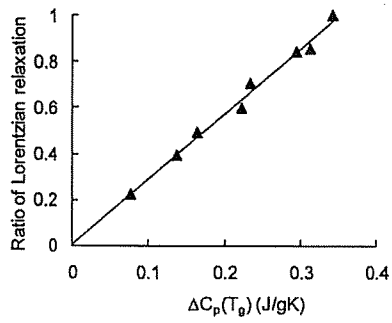


Fig. 6. The Ratio of FLF Fluorine Atoms Exhibiting Lorentzian Relaxation as a Function of Changes in the Heat Capacity at $T_g$

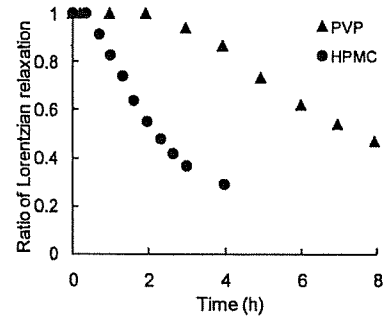


Fig. 7. Time Profiles of the Ratio of FLF Fluorine Atoms Exhibiting Lorentzian Relaxation in PVP and HPMC Solid Dispersions Stored at 60 °C

modynamic factors, such as free energy difference between crystalline and amorphous form.[2,3,10] Differences in the overall crystallization rate of amorphous FLF are consistent with those in the molecular mobility (Fig. 3), suggesting that the molecular mobility as determined by the $^{19}$F-NMR spin–lattice relaxation times may be one of the factors determining crystallization rate, and useful as a measure of the physical stability of FLF in solid dispersions. The $T_g$ values of the solid dispersions containing 20% PVP and 20% HPMC were 23 °C and 15 °C, respectively, indicating that molecular mobility reflected on $T_g$ is higher for the solid dispersion containing HPMC than for that containing PVP. The $T_g$ data seem to support the speculation obtained from NMR data. However, the scale of molecular mobility reflected on $T_g$ is considered to be larger than that reflected on $\tau_c$. Further studies should be conducted to elucidate the quantitative correlation between the physical stability of amorphous FLF and the molecular mobility determined by $^{19}$F-NMR.

In conclusion, $^{19}$F-NMR is useful for elucidating the molecular mobility of drugs containing fluorine atoms in amorphous solid dispersions. $\tau_c$ values of FLF fluorine atoms were calculated from the $^{19}$F-NMR spin–lattice relaxation data. The $\tau_c$ value for solid dispersions containing 20% PVP was 2—3 times longer than that for solid dispersions containing 20% HPMC at 50 °C. Molecular mobility of FLF in the solid dispersions containing 20% PVP was lower than in those containing 20% HPMC, and this was consistent with the fact that the overall crystallization rate of amorphous FLF in the solid dispersion containing PVP was smaller than in that containing HPMC. The molecular mobility determined by $^{19}$F-NMR seems to be useful as a measure of the physical stability of an amorphous drug in solid dispersions.

**Acknowledgements** Part of this work was supported by a Grant-in-aid for Research on Publicly Essential Drugs and Medical Devices from The Japan Health Sciences Foundation.

**References**

1) Yoshioka M., Hancock B. C., Zografi G., *J. Pharm. Sci.*, **84**, 983—986 (1995).
2) Matsumoto T., Zografi G., *Pharm. Res.*, **16**, 1722—1728 (1999).
3) Crowley K. J., Zografi G., *Pharm. Res.*, **20**, 1417—1422 (2003).
4) Shamblin S. L., Huang E. Y., Zografi G., *J. Therm. Anal.*, **47**, 1567—1579 (1996).
5) Shamblin S. L., Zografi G., *Pharm. Res.*, **16**, 1119—1124 (1999).
6) Zeng X. M., Martin G. P., Marriott C., *Int. J. Pharm.*, **218**, 63—73 (2001).
7) Miyazaki T., Yoshioka S., Aso Y., Kojima S., *J. Pharm. Sci.*, **93**, 2710—2717 (2004).
8) Khougaz K., Clas S., *J. Pharm. Sci.*, **89**, 1325—1334 (2000).
9) Berggren J., Alderborn G., *Eur. J. Pharm. Sci.*, **21**, 209—215 (2004).
10) Aso Y., Yoshioka S., Kojima S., *J. Pharm. Sci.*, **93**, 384—391 (2004).
11) Miyazaki T., Yoshioka S., Aso Y., *Chem. Pharm. Bull.*, **54**, 1207—1210 (2006).
12) Konno H., Taylor L. S., *J. Pharm. Sci.*, **95**, 2692—2705 (2006).
13) Aso Y., Yoshioka S., *J. Pharm. Sci.*, **95**, 318—325 (2006).
14) Harris R. K., Monti G. A., Holstein P., "Solid State NMR of Polymers," Chap. 6, ed. by Ando I., Asakura T., Elsevier, Amsterdam, 1998, pp. 351—414.
15) Grage S. L., Ulrich A. S., *J. Magn. Reson.*, **146**, 81—88 (2000).
16) Urano S., Matsuo M., Sakanaka T., Uemura I., Koyama M., Kumadaki I., Fukuzawa K., *Arch. Biochem. Biophys.*, **303**, 10—14 (1993).
17) Afonin S., Glaser R. W., Berditchevskaia M., Wadhwani P., Gührs K. H., Möllmann U., Perner A., Ulrich A. S., *ChemBioChem*, **4**, 1151—1163 (2003).
18) Salgado J., Grage S. L., Kondejewski L. H., Hodges R. S., McElhaney R. N., Ulrich A. S., *J. Biomol. NMR*, **21**, 191—208 (2001).
19) Williams S. P., Haggie P. M., Brindle K. M., *Biophys. J.*, **72**, 490—498 (1997).
20) Quint P., Ayala I., Busby S. A., Chalmers M. J., Griffin P. R., Rocca J., Nick H. S., Silverman D. N., *Biochemistry*, **45**, 8209—8215 (2006).
21) Farrar T. C., Breker E. D., "Pulse and Fourier Transform NMR," Academic Press, New York and Lodon, 1971.
22) Namgoong H., Lee J. W., *Bull. Korean Chem. Soc.*, **14**, 91—95 (1993).
23) Huang S.-G., Rogers M. T., *J. Chem. Phys.*, **68**, 5601—5606 (1978).
24) Gutowsky H. S., Lawrenceson I. J., Shimomura K., *Phys. Rev. Lett.*, **6**, 349—351 (1961).
25) Beckmann P. A., Rosenberg J., Nordstrom K., Mallory C. W., Mallory F. B., *J. Phys. Chem. A*, **110**, 3947—3953 (2006).
26) Horii F., "Solid State NMR of Polymers," Chap. 3, ed. by Ando I., Asakura T., Elsevier, Amsterdam, 1998, pp. 51—82.
27) Ruan R. R., Chen P. L., "Water in Foods and Biological Materials," Chap. 7, Technomic Publishing Co., Lancaster Basel, 1998, pp. 253—278.

Division of Drugs[1], National Institute of Health Sciences; Bruker Optics K.K.[2], Tokyo; TDDS Laboratory[3], Hisamitsu Pharmaceutical Co Inc, Ibaraki; Tokyo Metropolitan Industrial Technology Research Institute[4], Tokyo, Japan

# Chemical mapping of tulobuterol in transdermal tapes using Microscopic Laser Raman Spectroscopy

T. Sakamoto[1], T. Matsubara[2], D. Sasakura[2], Y. Takada[3], Y. Fujimaki[4], K. Aida[3], T. Miura[2], T. Terahara[3], N. Higo[3], T. Kawanishi[1], Y. Hiyama[1]

*Received July 29, 2008, accepted August 5, 2008*

*Tomoaki Sakamoto, Ph.D., National Institute of Health Sciences, 1-18-1, Kami-yoga, Setagaya-ku, Tokyo 158-8501, Japan*
*tsakamot@nihs.go.jp*

*Pharmazie 64: 166–171 (2009)* *doi: 10.1691/ph.2008.8217*

Microscopic Laser Raman Spectroscopy and Mapping (MLRSM) technique was used to investigate the distribution of tulobuterol (TBR) crystals in transdermal tapes. TBR is one of suitable compounds for the transdermal pharmaceuticals because it has high permeability into skin. In case of TBR transdermal tapes, some commercial products also contain TBR crystals in order to control a release rate from a matrix. Therefore, the presence of TBR crystals in the matrix is a critical factor for quality assurance of this type of TDDS tapes. The model tapes prepared here employed two kinds of matrices, i.e., rubber or acrylic, which are generally used for transdermal pharmaceuticals. TBR crystals in the matrix were observed by MLRSM. Accurate observation of the distribution of TBR in the tapes was achieved by creating a Raman chemical map based on detecting unique TBR peak in each pixel. Moreover, differences in the growth of TBR crystals in the two kinds of matrices were detected by microscopic observation. MLRSM also enabled the detection of TBR crystals in commercial products. The present findings suggest that Raman micro-spectroscopic analysis would be very useful for verifying and/or assessing the quality of transdermal pharmaceuticals in development, as well as for manufacturing process control.

## 1. Introduction

Tulobuterol (TBR) transdermal tapes are applied in cases of bronchial asthma as a bronchodilator ($\beta_2$-blocker). TBR suitable for use in transdermal drug delivery because it has high permeability into the keratin layer (Uematsu et al. 1993). TBR pharmaceutical products with a Transdermal Drug Delivery System (TDDS) have advantages such as eliminating the side effects including abdominal pain and appetite loss (Iikura et al. 1995), and maintaining effective blood TBR levels for approximately 24 h (Horiguchi et al. 2004). The release rate of TBR from the matrix is controlled by the formation of TBR crystals. The crystallization of TBR has the possibility of influencing the TBR blood level profile. Therefore, it is necessary to characterize not only the release rate of TBR from a matrix, but also to characterize its crystallinity in dosage form in the matrix. *In vitro* penetration testing using stripped animal skin and *in vitro* release testing have been used to evaluate transdermal pharmaceuticals in terms of penetration and release. Because these evaluation methods show only one of several alternative physicochemical parameters (e.g., release rate, rate of penetration rate of an active substance, etc.), it has remained difficult to clarify the chemical status and quality of transdermal pharmaceuticals. In case of transdermal tapes containing an active drug as crystals in a matrix, the active drug is slowly released from the matrix into the keratin layer, as crystals will gradually dissolve in a matrix. Therefore, the crystallization of TBR is an important quality parameter. However, evaluation of the correlation of release rates between animal skin and human skin using *in vitro* penetration testing of animal skin has also remained difficult. Therefore, it has become desirable to develop analytical methods of both microscopically and chemically detecting and observing crystals of active drugs in a matrix.

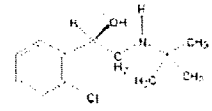

Tulobuterol (TBR)

Laser Raman spectroscopy is a method of spectroscopic analysis of spectra of Raman scattered light obtained by exposure of a sample to a laser. Raman spectroscopy has been used for the identification and quantification of polymorphs (Deely et al. 1991; Falcon et al. 2004; Ferrari et al. 2004; Findlay et al. 1998; Hu et al. 2005; Langkilde et al. 1997; Ono et al. 2004; Schöll et al. 2006; Starbuck et al. 2002; Wang et al. 2000; Murphy et al. 2005) and for monitoring the crystallization process (Taylor et al. 1998;

Murphy et al. 2005; Nørgaard et al. 2005) because it enables the detection of crystals, and in particular, differences between crystal forms. Therefore, Microscopic Laser Raman Spectroscopy/Mapping (MLRSM) was employed in the present study to microscopically and chemically detect TBR crystals in transdermal tapes. The applicability of this spectroscopic analytical method was examined both for the purpose of quality control (i.e., to confirm the crystals of TBR in the matrix), as well as with the aim of enhancing our understanding of relevant quality attributes of prototype pharmaceuticals in various stages of development.

## 2. Investigations and results

### *2.1. Determination of a unique wave number range in the Raman spectrum for TBR in model tapes*

A typical Raman spectrum obtained from the TBR reference standard substance is shown in Fig. 1. Typical spectra of placebo tape (a) and model tape (b) of rubber matrices are shown in Figs. 2 and 3, respectively. To find characteristic wave numbers of TBR, these spectra were compared with the Raman spectrum obtained from a model tape. The peak bending vibration of C–C at 415cm$^{-1}$ was used as the characteristic peak of TBR, and the integrated values obtained from the wave number range from 420 cm$^{-1}$ to 400 cm$^{-1}$ were used for making the Raman chemical maps.

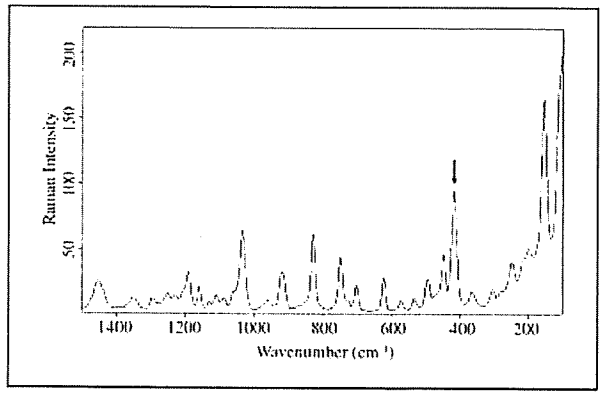


Fig. 1: Typical Raman spectrum of the TBR reference standard. The peak at 415 cm$^{-1}$ was chosen as characteristic, because no interfering peak was observed in the vicinity of this peak

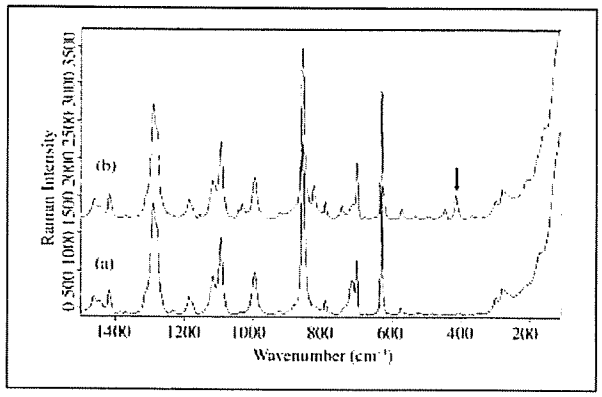


Fig. 2: Typical Raman spectra of placebo (a, rubber matrix) and model tape (b, rubber matrix). The arrow indicates the peak chosen for the specific detection of TBR. Comparatively strong intensity was observed

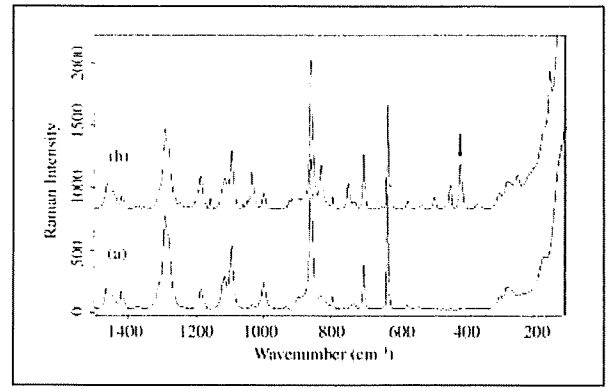


Fig. 3: Typical Raman spectra of placebo (a, acrylic matrix) and model tape (b, acrylic matrix). The very similar Raman spectrum of placebo tape was observed compared with that of the rubber matrix, because the absorption of supporting boards that were made from PET was also detected

### *2.2. Optical micrograph and Raman chemical mapping of the crystals of TBR in a rubber matrix*

Figure 4a shows the micrograph of a 600 × 500 µm area in the R-10 sample. An enlarged micrograph (200 × 200 µm) is shown in Fig. 4b. Pillar-shaped crystals (short, 1 µm–2 µm; long, 10 µm–20 µm) that formed in lumps were observed. Figure 4c and d show the three-dimensional (3D) map and the Raman chemical map that corresponds with the area in Fig. 4b. In the Raman chemical map, the distribution of TBR in the matrix corresponded with the distribution of crystals in the optical micrograph. The Raman absorbance intensity corresponded with the distribution of optically observed TBR.

### *2.3. Optical micrograph and Raman chemical mapping of the crystals of TBR in an acrylic matrix*

A micrograph of a 600 × 500 µm area and an enlarged micrograph of a 200 × 200 µm area of the A-20 sample are shown in Fig. 5a and b, respectively. In Figure 5c and d, the respective 3D chemical map and Raman chemical map are given that correspond to Fig. 5b. A lump of crystals with radiating branches was observed in the matrix. The Raman chemical map of TBR corresponding to the micrograph was obtained. The Raman chemical maps, which show the distribution of Raman chemical intensity, indicated trace amounts of crystal growth.

### *2.4. Shapes of crystals of TBR in two types of matrix*

The micrograph of early-stage TBR crystallization in an acrylic matrix is shown in Fig. 6a. A lump of crystals with radiating branches was observed. Figure 6b shows the micrograph obtained approximately at the level of the top of branch of the crystal. The findings suggest that the pillar-shaped crystals were successively generated at the top of branches, and that the branches grew radially from the core. In case of the rubber matrix, pillar-shaped crystals that formed individual lumps were observed, as shown in Fig. 4a and b. No signs of a core were observed, and lumps of pillar-shaped crystals occurred individually in the matrix. These findings suggest that the TBR crystal growth mechanism differs in the two types of matrix analyzed here. Empirical evidence suggests that when crystallization was rapid, numerous crystalline lumps lacking a nucleus appeared in all areas of the ma-

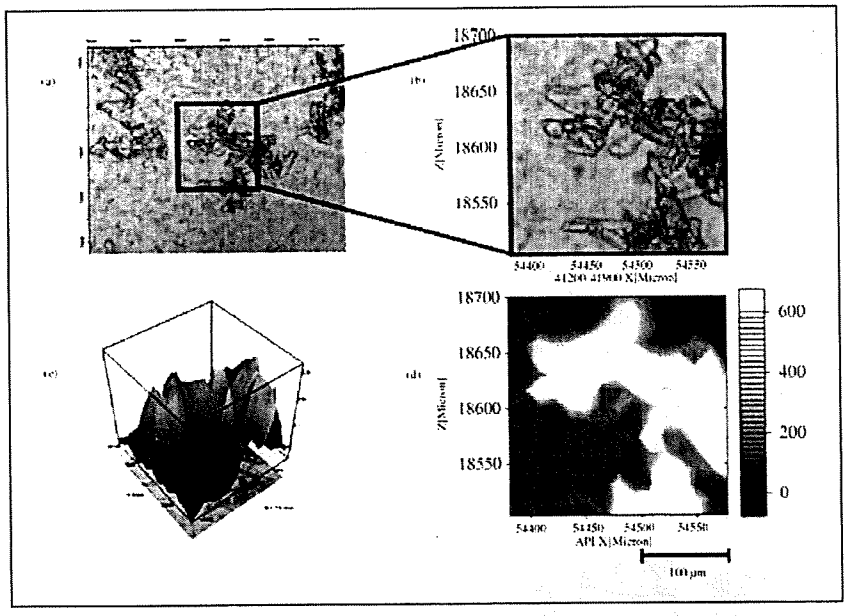


Fig. 4:
Micrographs and Raman chemical maps obtained from the model tape (R-10). a: Micrograph of a 600 × 500 µm area, b: Enlarged micrograph of a 200 × 200 µm area, c: 3D Raman chemical map that corresponds with that in d, d: Raman chemical map that corresponds with b. The distribution of the TBR crystals in the matrix was clearly detected by both methods

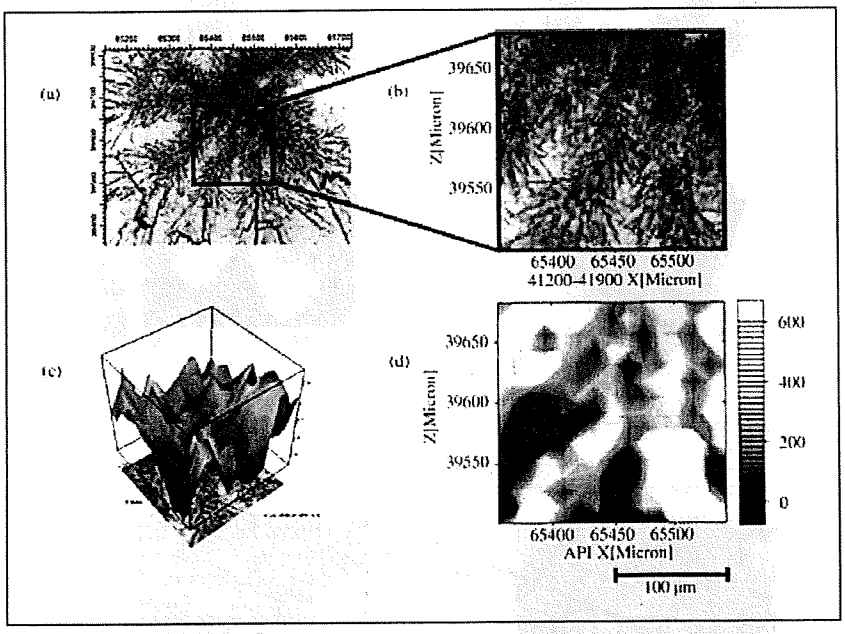


Fig. 5:
Micrographs and Raman chemical maps obtained from the model tape (A-20). a: Micrograph of a 600 × 500 µm area, b: Enlarged micrograph of a 200 × 200 µm area, c: 3D Raman chemical map that corresponds with d, d: Raman chemical map that corresponds with b. The mass of the crystals, with radiating branches, was observed in the matrix. The Raman chemical map of TBR corresponding to the micrograph was obtained

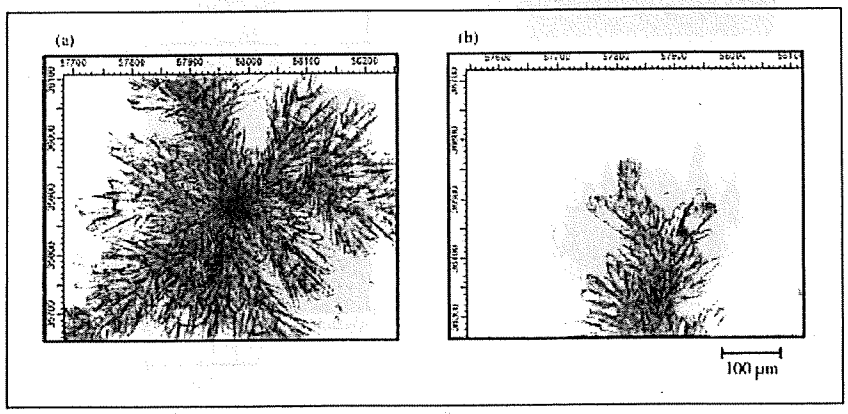


Fig. 6:
Micrographs of the mass of TBR crystals obtained from A-20. a: Core with radiating branches, b: Top of the branch. Pillar-shaped crystals generated successively at the top of branches were observed microscopically

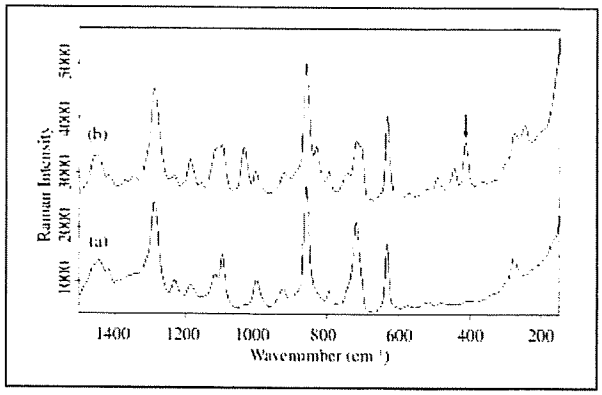


Fig. 7: Raman spectra of commercial tape. a: Background, b: The area where crystals were observed. The characteristic peak (415 $cm^{-1}$) of TBR was detected

trix, but in cases of slow crystallization, crystals formed around a nucleus. An empirical understanding of such processes would also suggest that the TBR crystals formed more rapidly in the rubber matrix than in the acrylic matrix. The processes of crystallization in these matrices agreed with the empirical evidence obtained here. It appears that new crystals will form around a nucleus, because surrounding molecules are stimulated to crystallize by a nucleus, as shown in Fig. 6. Raghavan et al. (2001) reported that the nucleation process depends in such cases on the hydrogen-bonding functional groups of not only the active drug, but also the polymer. Therefore, it appears likely that differences between the polymer structures of matrices contribute to differences in the process of crystal formation in those matrices. Although further study will still be needed to explain this phenomenon, it appears that the growth mechanism of TBR crystals in each matrix

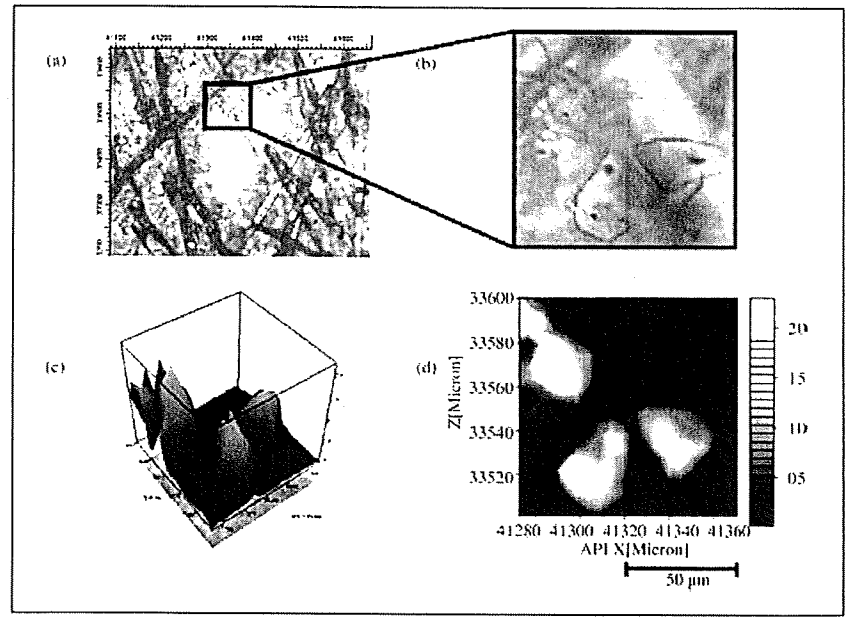


Fig. 8:
Micrographs and Raman chemical maps obtained from the commercial tape (1 mg TBR in the tape). a: Micrograph of a 570 × 450 µm area, b: Enlarged micrograph of a 100 × 100 µm area, c: 3D Raman chemical map that corresponds with d, d: Raman chemical map that corresponds with b. TBR crystals were clearly detected in the matrix

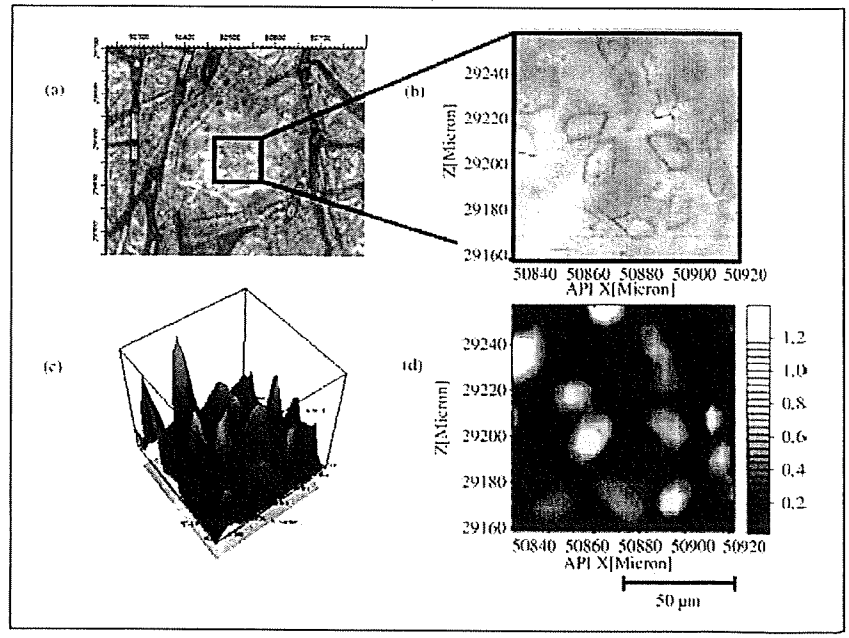


Fig. 9:
Micrographs and Raman chemical maps obtained from commercial tape (2 mg TBR in tape). a: Micrograph of a 570 × 450 µm area, b: Enlarged micrograph of a 100 × 100 µm area, c: 3D Raman chemical map that corresponds with d, d: Raman chemical map that corresponds with b. The crystal distribution suggested that rubber matrix was used for these products

may depend in part on hydrogen bonding between functional groups of TBR and the polymer.

### 2.5. Analysis of commercial products using MLRSM

MLRSM was used here to detect TBR crystals in commercial products. In these samples, there was a supporting board made of cloth, and a liner made of a white, plastic-like material. The tapes were measured after the liner was removed. Figure 7 shows the Raman spectra of commercial tape. Figure 7a or b were obtained from the area where crystals were not observed or the area where crystals were observed, respectively. The characteristic peak of TBR at 415 $cm^{-1}$ was detected. Figures 8 and 9 show the micrographs (a and b) and the Raman chemical maps (c and d) obtained from the commercial product, Hokunalin® tape, examined in 1 mg and 2 mg sizes, respectively. Areas in which TBR crystals were observed were selected for obtaining the Raman chemical maps. In both micrographs, more crystals appeared to be present in the 2 mg tape than in the 1 mg tape. However, according to the documentation for this product, several sizes of tape, prepared by cutting sections from a larger sheet, can yield various products. Therefore, the TBR content in a particular unit area in several types of Hokunalin® tapes will remain equivalent. It has been hypothesized that the number of crystals in a measured area is affected by the area selected for mapping. Moreover, TBR crystals were also observed that did not assume the lump-shaped formation in this product. Round, pillar-shaped crystals ranging in size from $6 \times 15$ μm to $30 \times 40$ μm were also observed. The formation of TBR crystals in the product was similar to that observed in a model tape made of a rubber matrix. Helpful information was provided in the attached documentation regarding the medical additives (e.g., polyisobutylene, polybutene, and lipocyclic petroleum resin) used to prepare the rubber matrix. The results of the present study suggest that the crystal formation patterns in a matrix yield useful information about unique matrix characteristics.

## 3. Discussion

The application of MLRSM to detect the crystals of an active drug in transdermal tapes has been studied. In the case of these TDDS pharmaceutical products, microscopy and chemical mapping method were useful for evaluating the quality of these products as non-destructive spectroscopic technology. Moreover, MLRSM could be used to measure products equipped with a liner for the purpose of quality control during processing, as well as to assess the crystallization of an active drug during storage. Non-destructive spectroscopic methods may be used for analysis of the chemical state and distribution of an active drug, not only in the case of transdermal tapes, but also in film-form products in pharmaceutical development. Furthermore, these methods could be applied as analytical tools to evaluate various factors affecting product quality in the manufacturing process.

## 4. Experimental

#### 4.1. Microscopic Laser Raman Spectroscopy and Mapping (MLRSM) instrument and measurement conditions

MLRSM measurement was performed using the SENTERRA Dispersive Raman Microscope (Bruker Optics K.K., Germany). Excitation wavelength, laser power, integration time, number of scans, spatial resolution and grating were set at 785 nm, 100 mW, 10 s, 1 scan, 2 μm and 1200 lines/mm, respectively.

#### 4.2. Materials

Tulobuterol (TBR, purity > 99.0%) was provided by Hisamitsu Pharmaceutical Co., Inc. (Tokyo, Japan). 2-Ethylhexyl acrylate vinylpyrrolidone copolymer, isopropyl myristate, polyisobutylene, polybutene, and lipocyclic petroleum resin for matrices of model patches were used as Japanese Pharmaceutical Excipients (JPE)-quality products. Hokunalin® Tape (1 mg and 2 mg) (Maruho Co. Ltd., Osaka, Japan) were purchased from a commercial source.

#### 4.3. Preparation of model tapes

Model tapes were prepared by the TDDS Laboratory, Hisamitsu Pharmaceutical Co., Inc. (Tsukuba, Japan). In order to identify crystalline lumps of TBR in the matrix, two types of matrix, rubber and acrylic, were prepared. TBR and other matrix adhesive solution ingredients were mixed and thoroughly stirred. The mixture was extended on a liner and residual solvents were removed by drying. The matrix was adjusted to a constant thickness (approximately 50 μm) and pasted onto a supporting board. A polyethylene terephthalate (PET) film was selected for the liner and the supporting board of the model tapes. Then, the sample was cut to a size of 36 mm diameter. TBR crystals in the model tapes were generated by leaving the sample to stand for one week (a rubber matrix) or one month (an acrylic matrix).

Model tapes were prepared that contained 0w/w% (R-0, placebo), and 10 w/w% (R-10) of TBR in a rubber matrix that consisted of polyisobutylene, polybutene, and lipocyclic petroleum resin. Small white crystals were seen in all areas of the matrix in the R-10 sample. Model tapes were prepared that contained 0 w/w% (A-0, placebo) and 20 w/w% (A-20) of TBR in an acrylic matrix composed of acrylic adhesive polymer and isopropyl myristate. Due to the solubility of TBR, higher TBR concentrations were necessary to generate crystals in the acrylic matrix than in the rubber matrix.

#### 4.4. Measurement of model tapes and commercial products

The model tapes with the liner were placed on a measurement stand with the liner side facing up. For the measurement of the model tapes, micrographs were obtained and chemical mapping was performed by microscopically focusing on crystals of interest. For the MLRSM measurements of the commercial TBR transdermal tapes, the tapes were placed without the liner on the measurement stand, with the adhesive side facing up.

Acknowledgement: This study was supported in part by a research grant from the Ministry of Health, Labour and Welfare (H17-iyaku-ippan-040).

**References**

Deely C, Spragg R, Threlfall T (1991) A Comparison of Fourier transform infrared and near-infrared Fourier transform Raman spectroscopy for quantitative measurements: an application in polymorphism. Spectrochim Acta 47: 1217–1223.

Falcon J, Berglund K (2004) In situ monitoring of antisolvent addition crystallization with principal components analysis of Raman spectra. Cryst Growth Des 4: 457–463.

Ferrari E, Davey R (2004) Solution-mediated transformation of α to β l-glutamic acid: rate enhancement due to secondary nucleation. Cryst Growth Des 4: 1061–1068.

Findlay P, Bugay D (1998) Utilization of Fourier transform-Raman spectroscopy for the study of pharmaceutical crystal forms. J Pharm Biomed Anal 16: 921–930.

Horiguchi T, Kondo R, Miyazaki J, Torigoe H, Tachikawa S (2004) Clinical evaluation of tulobuterol patch in patients with mild or moderate persistent bronchial asthma-effects of long-term treatment on airway inflammation and hypersensitivity. Nihon Kokyuki Gakkai Zasshi 42: 132–137.

Hu Y, Liang J, Myerson A, Taylor LS (2005) Crystallization monitoring by Raman spectroscopy: simultaneous measurement of desupersaturation profile and polymorphic form in flufenamic acid systems. Ind Eng Chem Res 44: 1233–1240.

Iikura Y, Uchiyama H, Akimoto K, Ebisawa M, Sakaguchi N, Tsubaki T, Ishizu H, Kabayama H, Yagi K, Miura K (1995) Pharmacokinetics and pharmacodynamics of the tulobuterol patch, HN-078, in childhood asthma. Ann Allergy Asthma Immunol 74: 147–151.

Langkilde F, Sjöblom J, Tekenbergs-Hjelte L, Mrak A (1997) Quantitative FT-Raman analysis of two crystal forms of a pharmaceutical compound. J Pharm Biomed Anal 15: 687–696.

Murphy BM, Prescott SW, Larson I (2005) Measurement of lactose crystallinity using Raman spectroscopy. J Pharm Biomed Anal 38: 186–190.

Nørgaard L, Hahn MT, Knudsen LB, Farhat IA, Engelsen SB (2005) Multivariate near infrared and Raman spectroscopic quantifications of the crystallinity of lactose in whet permeate powder. Int Dairy J 15: 1261–1270.

Ono T, ter Horst J, Jansens P (2004) Quantitative measurement of the polymorphic transformation of l-glutamic acid using in-situ Raman spectroscopy. Cryst Growth Des 4: 465–469.

Raghavan SL, Trividic A, Davis AF, Hadgraft J (2001) Crystallization of hydrocortisone acetate: influence of polymers. Int J Pharm 212: 213–221.

Schöll J, Bonalumi D, Vicum L, Mazzotti M (2006) In situ monitoring and modeling of the solvent-mediated polymorphic transformation of l-glutamic acid. Cryst Growth Des, 6: 881–891.

Starbuck C, Spartails A, Wai L, Wang J, Fernandez P, Lindemann C, Zhou G, Ge Z (2002) Process optimization of a complex pharmaceutical polymorphic system via in situ Raman spectroscopy. Cryst Growth Des 2: 515–522.

Taylor LS, Zografi G (1998) Quantitative analysis of crystallinity using FT-Raman spectroscopy. Pharm Res 15: 755–761.

Uematsu T, Nakano M, Kosuge K, Kanamaru M, Nakashima M (1993) The pharmacokinetics of the beta 2-adrenocepter agonist, tulobuterol given transdermally and by inhalation. Eur J Clin Pharmacol 44: 361–364.

Wang F, Wachter J, Antosz F, Berglund K (2000) An investigation of solvent-mediated polymorphic transformation of progesterone using in situ Raman spectroscopy. Org Proc Res Dev, 4: 391–395.

AAPS PharmSciTech, Vol. 10, No. 2, June 2009 (© 2009)
DOI: 10.1208/s12249-009-9243-0

*Research Article*

# Near-Infrared Analysis of Hydrogen-Bonding in Glass- and Rubber-State Amorphous Saccharide Solids

**Ken-ichi Izutsu,[1,2] Yukio Hiyama,[1] Chikako Yomota,[1] and Toru Kawanishi[1]**

*Received 17 October 2008; accepted 9 April 2009; published online 7 May 2009*

***Abstract.*** Near-infrared (NIR) spectroscopic analysis of noncrystalline polyols and saccharides (e.g., glycerol, sorbitol, maltitol, glucose, sucrose, maltose) was performed at different temperatures (30–80°C) to elucidate the effect of glass transition on molecular interaction. Transmission NIR spectra (4,000–12,000 $cm^{-1}$) of the liquids and cooled-melt amorphous solids showed broad absorption bands that indicate random configuration of molecules. Heating of the samples decreased an intermolecular hydrogen-bonding OH vibration band intensity (6,200–6,500 $cm^{-1}$) with a concomitant increase in a free and intramolecular hydrogen-bonding OH group band (6,600–7,100 $cm^{-1}$). Large reduction of the intermolecular hydrogen-bonding band intensity at temperatures above the glass transition ($T_g$) of the individual solids should explain the higher molecular mobility and lower viscosity in the rubber state. Mixing of the polyols with a high $T_g$ saccharide (maltose) or an inorganic salt (sodium tetraborate) shifted both the glass transition and the inflection point of the hydrogen-bonding band intensity to higher temperatures. The implications of these results for pharmaceutical formulation design and process monitoring (PAT) are discussed.

**KEYWORDS:** amorphous; glass transition; hydrogen-bonding; NIR; PAT.

## INTRODUCTION

The development of amorphous solid pharmaceutical formulations requires thorough characterization of physical properties (1–4). Optimizing the molecular mobility and the system viscosity, which both change significantly at glass transition temperature ($T_g$), is essential to ensure their unique functional characters (e.g., faster dissolution of active ingredients, stabilization of lyophilized protein conformation) and storage stability of these solids. Understanding how the molecular interactions, particularly hydrogen-bonding, in amorphous carbohydrate solids affect their physical properties is relevant to the formulation design and process control (5).

Near-infrared (NIR) spectroscopy is an advancing analytical method that provides varied information on the chemical and physical properties of pharmaceutical formulations including molecular structure, crystallinity (6–8), crystal polymorphs (9,10), residual water content (11), component miscibility (12), protein secondary structure (13), and molecular interactions (14–17). Relatively low absorbance that enables diffuse-reflection measurement and recent advances in chemometrics (e.g., principal component analysis [PCA], partial least-squares calibration [PLS]) make the NIR spectroscopy a powerful nondestructive process analytical tool for quality control (PAT) (18). The applicability of vacuum-sealed samples in glass vials should be an apparent advantage of NIR in the analysis of physically unstable amorphous solids. Proper use of NIR spectroscopy, combined with other sophisticated in-, on-, and at-line analytical tools (e.g., mid-infrared, far-infrared, terahertz, and Raman spectroscopy; thermal analysis), should improve the product and process understanding required for better formulation quality (16,19,20).

The purpose of this study was to characterize hydrogen-bonding profiles in rubber- and glass-state amorphous solids by NIR spectroscopy. The random configuration of molecules and the accompanying wide variation of molecular interactions in amorphous polyol and saccharide solids provide broad absorption bands in the NIR spectra (6,7). Some of the broad bands (e.g., OH stretching vibration) indicate different hydrogen-bonding states (e.g., intermolecular, intramolecular, free) in the solids (21,22). The profiles of the hydrogen-bonding in water and some alcohol liquids depend largely on temperature (23–25). Recent mid-infrared studies on the amorphous saccharide films indicate different temperature-dependent shifts of OH stretching (3,300–3,400 $cm^{-1}$) and bending (1,000–1,100 $cm^{-1}$) vibration band peaks between their glass (below $T_g$) and rubber (above $T_g$) states (26,27). It is plausible that NIR spectroscopy provides valuable information on the molecular interactions and physical properties of various noncrystalline samples (e.g., liquid, rubber-state solid, glass-state solid).

[1] National Institute of Health Sciences, Kamiyoga 1-18-1, Setagaya, Tokyo 158-8501, Japan.
[2] To whom correspondence should be addressed. (e-mail: izutsu@nihs.go.jp)

## MATERIALS AND METHODS

### Materials

All chemicals employed in this study were of analytical grades and were obtained from the following commercial sources: glycerol and sorbitol (Wako Pure Chemical, Osaka, Japan); maltose monohydrate, sucrose, and sodium tetraborate (Sigma Chemical, St. Louis, MO, USA); deuterium water (Acros Organics, Geel, Belgium); maltitol and maltotriitol (Hayashibara Biochemical Laboratories, Okayama, Japan).

### Preparation of Freeze-Dried Amorphous Solids

Freeze-dried solids were prepared by lyophilizing aqueous polyol and saccharides solutions (100 mg/mL, 2 mL) in flat-bottom borosilicate glass vials (21 mm diameter; SVF-10, Nichiden-rika Glass, Kobe, Japan) using a Freezevac-1C freeze-drier (Tozai Tsusho, Tokyo, Japan). The sample solutions frozen by immersion in liquid nitrogen were dried under vacuum without temperature control for 16 h and then maintained on the shelf at 35°C for 8 h. Hydrogen/deuterium-exchanged glycerol, sorbitol, and glucose were obtained by freeze-drying the solutions in $D_2O$ twice (200 mg/mL).

### Preparation of Cooled-Melt Amorphous Solids

The cooled-melt solids subjected to thermal and NIR analysis were obtained by melting the crystalline powder in a quartz cuvette (1-mm light path length; Starna Optiglass, Hainault, UK) or small borosilicate glass tubes (approximately 4 mm internal diameter; TGK, Tokyo, Japan) in a drying oven (DP23, Yamato Scientific, Tokyo, Japan) at 200°C (sucrose) or 180°C (other saccharides) under vacuum for 20 min, then cooled at room temperature. Amorphous maltose solids were prepared from the monohydrate crystal with (dehydrated) or without (partially hydrated) vacuum-drying. The cooled-melt solids without apparent crack or bubbles were subjected to the following transmission NIR analysis.

### Thermal Analysis

A differential scanning calorimeter (DSC Q-10, TA Instruments, New Castle, DE, USA) and software (Universal Analysis 2000, TA Instruments) were used to obtain the thermal properties of the amorphous solids. Solids (2–5 mg) in hermetic aluminum cells were scanned from −30°C at 5°C/min under $N_2$ gas flow. Glass transition temperatures were determined from the maximum inflection point of the discontinuities in the heat flow curves.

### NIR Spectroscopy

NIR analysis was performed using a FT-NIR system (MPA, Bruker Optik, Germany) equipped with a sample temperature controller and OPUS software. Transmission NIR spectra of liquids and cooled-melt amorphous solids were obtained from 30°C to 80°C at every 5°C with 5-min intervals between the measurements. Absorbance in the 12,000 to 4,000 $cm^{-1}$ range was obtained with a 2-$cm^{-1}$ resolution in 128 scans. The absorbance of air was subtracted as background. The NIR spectra were baseline-corrected in the 8,000–9,000 $cm^{-1}$ range and smoothed at 25 points. The possible effect of a temperature-induced solid volume change was not compensated in this study. Diffuse-reflection NIR spectra of crystal powders and freeze-dried solids in cylindrical borosilicate glass vials were obtained from the bottom of the container at room temperature.

## RESULTS

Figure 1 shows the diffuse-reflection NIR spectra of mannitol, maltose monohydrate, sucrose, glucose, and sorbitol in different physical states (crystalline powder, freeze-dried solid) obtained noninvasively from the bottoms of the glass vials. The crystalline powders showed several unique sharp bands of OH and CH vibrations in the overtone (5,000–7,500 $cm^{-1}$) and combination (4,000–5,000 $cm^{-1}$) spectral regions. The absorbance of water in the maltose monohydrate crystal (around 5,150 $cm^{-1}$) disappeared by lyophilization. Freeze-dried amorphous sucrose and maltose solids showed broad absorption bands that indicate diversified interactions between the spatially less-ordered molecules. Contrarily, some sharp peaks (e.g., 4,375 $cm^{-1}$) indicated partial crystallinity of the freeze-dried mannitol (4,28). Thermal analysis of the freeze-dried solids also indicated different component crystallinity (data not shown). Freeze-drying of glucose and sorbitol resulted in collapsed solids, which spectra varied largely between the vials (data not shown). Amorphous saccharide solids prepared by cooling the heat-melt also showed varied diffuse-reflection NIR spectra.

Transmission NIR analysis of cooled-melt amorphous solids (e.g., sorbitol, glucose) and a liquid (glycerol) in a quartz cell (1-mm light path length, 30°C) showed similar spectra with some broad bands (Fig. 2A). The large bands in

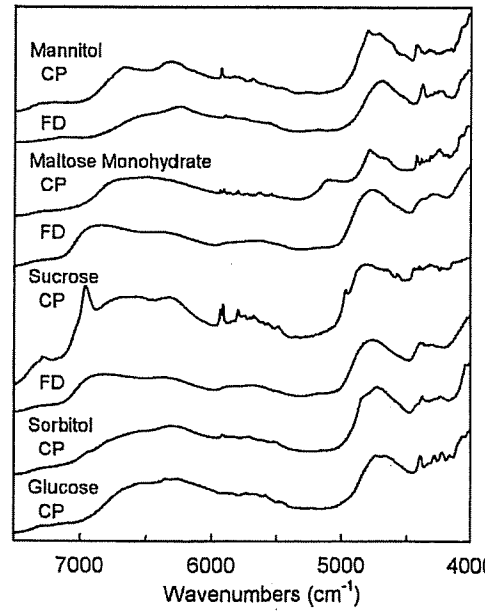


**Fig. 1.** Diffuse-reflection NIR spectra of crystalline powder (*CP*) and freeze-dried solid (*FD*) containing sugars and sugar alcohols obtained at the bottoms of glass vials

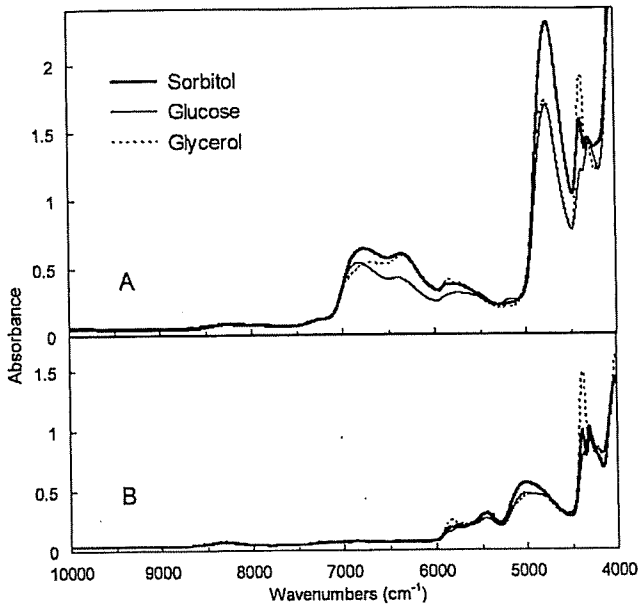


**Fig. 2.** Transmission NIR spectra of liquid (glycerol) and cooled-melt solids (sorbitol, glucose) in a quartz cell (1-mm light path length) prepared with **A** without and **B** with hydrogen/deuterium exchange (30°C)

the overtone spectral region represent OH stretching vibration first overtones of intermolecular hydrogen-bonding groups (6,200–6,500 $cm^{-1}$) and intramolecular or nonhydrogen-bonding groups (6,600–7,100 $cm^{-1}$) (21,22,25). The addition of $H_2O$ (2–10%, *w/w*) to glycerol increased the absorbance at around 4,110, 5,152, and 6,925 $cm^{-1}$ in the NIR spectra (data not shown). Hydrogen/deuterium-exchanged samples showed a large band that suggested an OD stretching vibration at around 5,000 $cm^{-1}$ (Fig. 2B) (23). Lower absorbance of the hydrogen/deuterium-exchanged amorphous solids at 6,000–7,100 $cm^{-1}$ confirmed the significance of the OH stretching vibration band in the spectral region. Thermal analysis showed that the cooled-melt sorbitol ($T_g$=−1.2°C) and glucose ($T_g$= 45.8°C) are in the rubber and glass states, respectively, at 30°C.

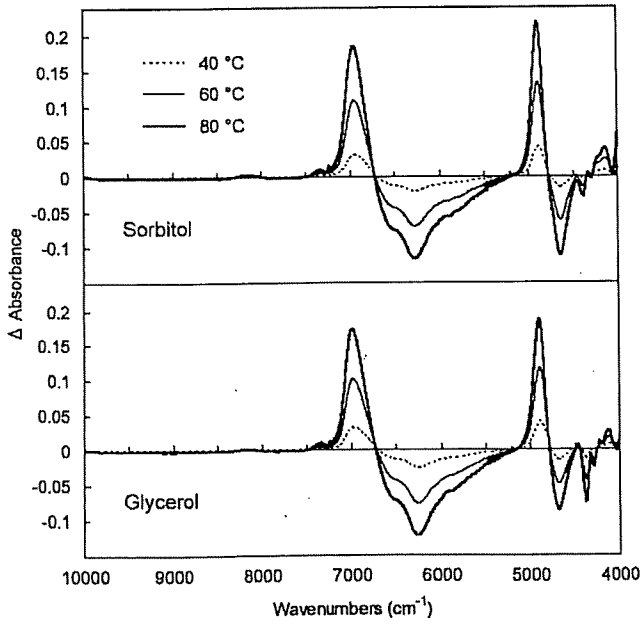


**Fig. 3.** Effect of heating on the transmission NIR spectra of glycerol liquid and cooled-melt sorbitol solid (1-mm light path length). Difference spectra were obtained by subtracting the absorbance of the samples at 30°C

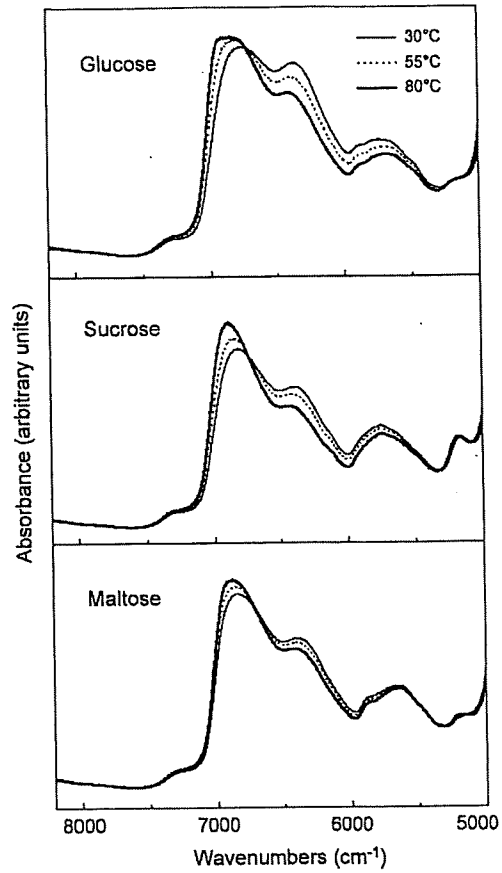


**Fig. 4.** Transmission NIR spectra of cooled-melt amorphous glucose, sucrose, and maltose (dehydrated) solids in glass tubes (approximately 4 mm interior diameter) obtained at 30°C, 55°C, and 80°C

The effect of heating on the transmission NIR spectra of the noncrystalline sorbitol and glycerol are shown as the difference spectra (Fig. 3). The changes indicated the shift of the major bands at 6,000–7,000 $cm^{-1}$ (OH stretching vibration first overtone) and at around 4,750 $cm^{-1}$ (OH stretching/bending combination) in the original spectra to higher wave numbers at the elevated temperatures (40°C, 60°C, and 80°C). The apparent decrease in the absorbance at 6,000–6,500 $cm^{-1}$ and the concomitant absorbance increase at 6,700–7,100 $cm^{-1}$ suggested heat-induced changes in the hydrogen-bonding profiles of the OH groups from intermolecular to intramolecular or free bonds.

Transmission NIR spectra (overtone region) of cooled-melt glucose, sucrose, and maltose (dehydrated) obtained at different temperatures (30°C, 55°C, and 80°C) suggested varied heat-induced changes in the hydrogen-bonding band intensity (Fig. 4). The larger spectral change observed in the lower glass transition temperature solids (glucose=45.8°C) suggested the contribution of the different hydrogen-bonding profiles to the physical properties. The solids were prepared

in small glass tubes (approximately 4 mm internal diameter) to prevent crack formation in the cooling process. The browning of sucrose during the preparation indicated its partial degradation at high temperatures. A small absorption band at 5,150 $cm^{-1}$ suggested residual water in the amorphous saccharide solids. Relatively large absorbance at the 6,200- to 6,500-$cm^{-1}$ region in the amorphous glucose solid suggested a larger contribution of the intermolecular hydrogen-bonding compared to those in other saccharides. Different dehydration process and accompanying changes in the molecular interactions should explain the partially different spectra of the cooled-melt glucose solid prepared in the quartz optical cell (Fig. 2) and the glass tube (Fig. 4).

The relationship between the hydrogen-bonding profiles and the physical states of the amorphous solids were further studied. Thermal analysis showed varied glass transition temperatures of the cooled-melt amorphous polyol and saccharide solids (Table I). The changes in the absorbance of the intermolecular hydrogen-bonding OH band peak (6,200–6,500 $cm^{-1}$) obtained every 5°C were plotted in Fig. 5. The spectral region was chosen for comparison because of the smaller overlapping absorbance of residual water compared to that in the intramolecular hydrogen-bonding band region (6,600–7,100 $cm^{-1}$) (11). The noncrystalline samples showed three types of intermolecular hydrogen-bonding band intensity changes depending on their glass transition temperatures. A rubber-state solid (sorbitol, $T_g$=−1.2°C) and glycerol liquid showed relatively large (<0.04 U/5°C) band intensity drops from the lowest measurement temperature. Contrarily, amorphous dehydrated maltose that remained in the glass state throughout the measurement temperature range (80°C< $T_g$) showed a much smaller band intensity change. Other solids (e.g., glucose, sucrose, maltotriitol; 30°C<$T_g$<80°C) showed larger declines of the band intensity above their glass transition temperatures. Plotting of the band intensity against the temperature showed apparent inflection at the glass transition. Plateau of the plot above the $T_g$ should indicate large and constant temperature-dependent reduction of the molecular interactions similar to that of molecular liquids.

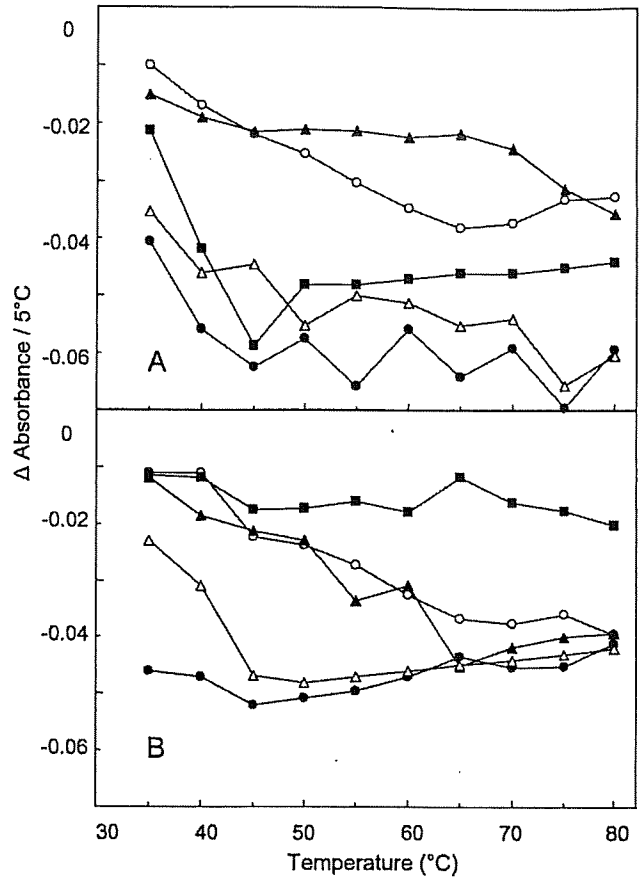


**Fig. 5.** Changes in the absorbance of intermolecular hydrogen-bonding OH vibration band obtained by transmission NIR scan of noncrystalline samples at 5°C intervals. Each point of the curves represents the mean of duplicated measurements. Each symbol denotes **A** glycerol (*filled circles*), sorbitol (*open triangles*), glucose (*filled squares*), sucrose (*open circles*), maltotriitol (*filled triangles*) and **B** maltose (*filled squares*), maltose hydrate (*open circles*), and maltose+sorbitol at the weight ratios of 2:1 (*filled circles*), 3:1 (*open triangles*), and 5:1 (*filled triangles*)

**Table I.** Glass Transition Temperature of Cooled-Melt Amorphous Solids

| Glass transition temperatures | |
|---|---|
| Maltose | 99.4±1.2 |
| Maltotriitol | 79.5±0.8 |
| Maltose (w/o vacuum-drying) | 62.6±1.7 |
| Sucrose | 57.9±3.2 |
| Maltitol | 49.3±0.5 |
| Glucose | 45.8±2.2 |
| Glycerol (liquid) | n.d. |
| Sorbitol | −1.2±0.9 |
| Maltose+sorbitol 5:1[a] | 66.5±1.9 |
| Maltose+sorbitol 3:1[a] | 48.6±0.5 |
| Maltose+sorbitol 2:1[a] | 31.0±0.3 |
| Maltitol+$Na_2B_4O_7$ 40:1[b] | 59.0±2.1 |
| Maltitol+$Na_2B_4O_7$ 25:1[b] | 69.2±1.7 |

Data are presented as mean±SD ($n$=3)
[a] Weight ratio
[b] Molar ratio

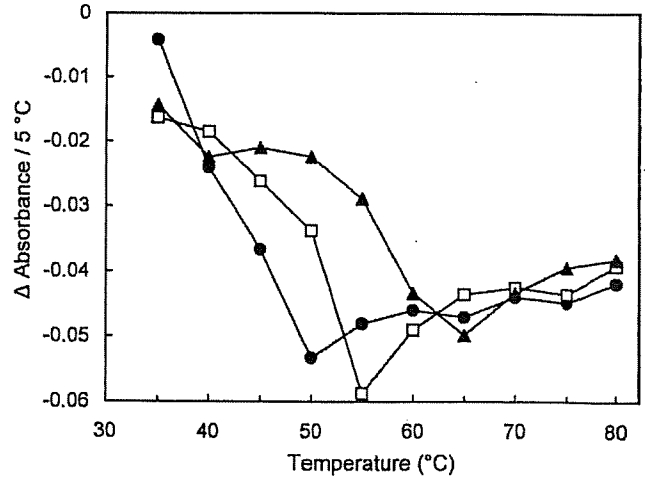


**Fig. 6.** Effect of temperature on the intermolecular hydrogen-bonding OH vibration band absorbance of maltitol (*filled circles*) and its mixture with $Na_2B_4O_7$ at the molar ratio of 40:1 (*open squares*) and 25:1 (*filled triangles*) obtained at 5°C intervals ($n$=2)

Some solids containing multiple components also showed larger heat-induced reduction of the intermolecular hydrogen-bonding band in the rubber state. The mixing of components (e.g., maltose and sorbitol) or higher residual water (e.g., cooled-melt maltose monohydrate prepared without vacuum-drying) shifts the glass transition temperature of the amorphous solids (Table I). These solids showed larger heat-induced intermolecular hydrogen-bonding band intensity reductions at above their glass transition temperatures (Fig. 5). Some inorganic salts (e.g., sodium phosphates, sodium citrates) affect the glass transition temperature of amorphous polyol and saccharide solids (29,30). The addition of a small amount of sodium tetraborate ($Na_2B_4O_7$) significantly raised the $T_g$ of cooled-melt maltitol solids (Table I), as well as the inflection temperature of the intermolecular hydrogen-bonding band intensity (Fig. 6) (31,32).

## DISCUSSION

The NIR study showed varied hydrogen-bonding states of OH groups in the noncrystalline polyol and saccharide solids that depended both on their temperatures and their physical states (glass and rubber). The heating-induced reduction of the intermolecular hydrogen bond was consistent with the literature on the NIR analysis of water, alcohol, and polyol liquids (25,33). The limited absorbance of hydrogen/deuterium-exchanged polyols (glucose, sorbitol) at above 6,000 $cm^{-1}$ indicated the contribution of readily exchangeable OH groups to the temperature-dependent band intensity change. The appropriate sample temperature control and the constant light path length made the transmission NIR measurement suitable to study the relationship between the physical states and the molecular interactions. The general trends observed in the transmission mode should be basically applicable to other data detection modes (e.g., diffuse-reflection).

The glass transition of the amorphous solids did not directly affect the NIR spectra, but it altered the extent of the heat-induced hydrogen-bonding band intensity change. The result was in agreement with the different temperature-dependent changes in the mid-infrared OH stretching and bending band peak positions of saccharide films in the glass and rubber states (26,27). Loosening of the intermolecular hydrogen-bonding network should induce the higher molecular mobility and lower viscosity of the rubber-state amorphous solids. The rubber-state amorphous solids are, from another physical perspective, deeply supercooled liquids with extremely high viscosity. The similarity in physical states would explain the large constant heat-induced reduction of the intermolecular band intensity in the polyol liquids (e.g., glycerol) and the rubber-state solids. The smaller heat-induced spectral changes below the $T_g$ would increase the mobility of molecules, leading to slow but not negligible temperature-dependent chemical degradation and/or ingredient crystallization in the long-term storage of the glass-state amorphous solids (34). Further assignment of the bands in the NIR spectra and mathematical data processing should increase the relevance of the analysis.

Information on the molecular interactions (e.g., hydrogen-bonding) that determine the physical properties should be relevant for the rational design of amorphous formulations. NIR spectroscopy should be used to characterize the molecular interactions in certain multicomponent amorphous systems containing the active pharmaceutical ingredients, excipients (e.g., stabilizer, pH modifier), and residual water. The availability of several detection modes that involve samples in glass containers without exposure to unfavorable environments (e.g., humid atmosphere) is a major advantage of NIR spectroscopy over other analytical methods for the characterization of the amorphous freeze-dried formulations (15). The proper choice of excipients that form and/or induce intermolecular hydrogen-bonding (e.g., disaccharides, sodium phosphate) should provide the storage stability and functional properties required for the amorphous formulations.

NIR spectroscopy is a powerful analytical tool for process monitoring and raw material inspection (18,20). Ensuring chemical and physical properties during the process is important to obtain reliable pharmaceutical formulations. Clinical functions and storage stabilities of the amorphous solid formulations depends not only on their glass transition temperatures ($T_g$) but also on other physical characters (e.g., residual crystallinity, structural relaxation) that are affected by process parameters (e.g., thermal history) (3). Several mathematical data processing methods, including PLS and PCA, have been used to obtain information on the chemical and physical properties of solids (e.g., crystallinity, collapse, residual water, chemical degradation) from the NIR spectra. The preparation of amorphous solids often includes low (e.g., freeze-drying) or high (e.g., melting, extrusion) temperature processes. Understanding the effect of temperature and physical states on the NIR spectra, as well as appropriate data compensation, should increase the relevance of the sophisticated analytical methods.

## ACKNOWLEDGEMENT

The present study was supported by the Japan Health Sciences Foundation (KH31029, KHB1006).

## REFERENCES

1. Cui Y. A material science perspective of pharmaceutical solids. Int J Pharm. 2007;339:3–18.
2. Hancock BC, Zografi G. Characteristics and significance of the amorphous state in pharmaceutical systems. J Pharm Sci. 1997;86:1–12.
3. Hilden LR, Morris KR. Physics of amorphous solids. J Pharm Sci. 2004;93:3–12.
4. Nail SL, Jiang S, Chongprasert S, Knopp SA. Fundamentals of freeze-drying. Pharm Biotechnol. 2002;14:281–360.
5. Tang XC, Pikal MJ, Taylor LS. The effect of temperature on hydrogen bonding in crystalline and amorphous phases in dihydropyrine calcium channel blockers. Pharm Res. 2002;19:484–90.
6. Yonemochi E, Inoue Y, Buckton G, Moffat A, Oguchi T, Yamamoto K. Differences in crystallization behavior between quenched and ground amorphous ursodeoxycholic acid. Pharm Res. 1999;16:835–40.
7. Hogan SE, Buckton G. The application of near infrared spectroscopy and dynamic vapor sorption to quantify low amorphous contents of crystalline lactose. Pharm Res. 2001;18:112–6.
8. Seyer JJ, Luner PE, Kemper MS. Application of diffuse reflectance near-infrared spectroscopy for determination of crystallinity. J Pharm Sci. 2000;89:1305–16.
9. Otsuka M, Kato F, Matsuda Y. Comparative evaluation of the degree of indomethacin crystallinity by chemoinfometrical Four-

ier-transformed near-infrared spectroscopy and conventional powder X-ray diffractometry. AAPS PharmSci. 2000;2:E9.
10. Tudor AM, Church SJ, Hendra PJ, Davies MC, Melia CD. The qualitative and quantitative analysis of chlorpropamide polymorphic mixtures by near-infrared Fourier transform Raman spectroscopy. Pharm Res. 1993;10:1772–6.
11. Stein HH, Ambrose JM. Near-infrared method for determination of water in aluminum aspirin. Anal Chem. 1963;35:550–2.
12. Jovanović N, Gerich A, Bouchard A, Jiskoot W. Near-infrared imaging for studying homogeneity of protein–sugar mixtures. Pharm Res. 2006;23:2002–13.
13. Bai S, Nayar R, Carpenter JF, Manning MC. Noninvasive determination of protein conformation in the solid state using near infrared (NIR) spectroscopy. J Pharm Sci. 2005;94:2030–8.
14. Izutsu K, Fujimaki Y, Kuwabra A, Aoyagi N. Effect of counterions on the physical properties of L-arginine in frozen solutions and freeze-dried solids. Int J Pharm. 2005;301:161–9.
15. Liu J. Physical characterization of pharmaceutical formulations in frozen and freeze-dried solid states: techniques and applications in freeze-drying development. Pharm Dev Technol. 2006;11: 3–28.
16. Räsänen E, Sandler N. Near infrared spectroscopy in the development of solid dosage forms. J Pharm Pharmacol. 2007;59: 147–59.
17. Reich G. Near-infrared spectroscopy and imaging: basic principles and pharmaceutical applications. Adv Drug Deliv Rev. 2005;57: 1109–43.
18. Fevotte G, Calas J, Puel F, Hoff C. Applications of NIR spectroscopy to monitoring and analyzing the solid state during industrial crystallization processes. Int J Pharm. 2004;273:159–69.
19. FDA. Guidance for industry: PAT—a framework for innovative pharmaceutical development, manufacturing and quality assurance. http://www.fda.gov/cder/guidance/6419fnl.htm (2004)
20. De Beer TR, Allesø M, Goethals F, Coppens A, Heyden YV, De Diego HL, et al. Implementation of a process analytical technology system in a freeze-drying process using Raman spectroscopy for in-line process monitoring. Anal Chem. 2007;79:7992–8003.
21. Ozaki Y, Kawata S. Near-infrared spectroscopy. Tokyo: Japan Scientific Societies Press; 1996.
22. Shenk JS, Workman JJ Jr., Westerhaus MO. Application of NIR spectroscopy to agricultural products. In: Burns DA, Ciurczak WW, editors. Handbook of near-infrared analysis. New York: Taylor & Francis; 2001. p. 419–74.
23. Czarnecki MA, Czarnik-Matusewicz B, Ozaki Y, Iwahashi M. Resolution enhancement and band assignments for the first overtone of OH(D) stretching modes of butanols by two-dimensional near-infrared correlation spectroscopy. 3. Thermal dynamics of hydrogen bonding in butan-1-(ol-d) and 2-methylpropan-2-(ol-d) in the pure liquid states. J Phys Chem A. 2000;104:4906–11.
24. Czarnecki MA, Ozaki Y. The temperature-induced changes in hydrogen bonding of decan-1-ol in the pure liquid phase studied by two-dimensional Fourier transform near-infrared correlation spectroscopy. Phys Chem Chem Phys. 1999;1:797–800.
25. Maeda H, Ozaki Y. Near infrared spectroscopy and chemometrics studies of temperature-dependent spectral variations of water: relationship between spectral changes and hydrogen bonds. J Near Infrared Spectrosc. 1995;3:191–201.
26. Wolkers WF, Oldenhof H, Alberda M, Hoekstra FA. A Fourier transform infrared microspectroscopy study of sugar glasses: application to anhydrobiotic higher plant cells. Biochim Biophys Acta. 1998;1379:83–96.
27. Wolkers WF, Oliver AE, Tablin F, Crowe JH. A Fourier-transform infrared spectroscopy study of sugar glasses. Carbohydr Res. 2004;339:1077–85.
28. Cao W, Mao C, Chen W, Lin H, Krishnan S, Cauchon N. Differentiation and quantitative determination of surface and hydrate water in lyophilized mannitol using NIR spectroscopy. J Pharm Sci. 2006;95:2077–86.
29. Ohtake S, Schebor C, Palecek SP, Pablo JJD. Effect of pH, counter ion, and phosphate concentration on the glass transition temperature of freeze-dried sugar–phosphate mixtures. Pharm Res. 2004;21:1615–21.
30. Kets EP, IJpelaar PJ, Hoekstra FA, Vromans H. Citrate increases glass transition temperature of vitrified sucrose preparations. Cryobiology 2004;48:46–54.
31. Miller DP, Anderson RE, de Pablo JJ. Stabilization of lactate dehydrogenase following freeze thawing and vacuum-drying in the presence of trehalose and borate. Pharm Res. 1998;15:1215–21.
32. Izutsu K, Yomota C, Aoyagi N. Inhibition of mannitol crystallization in frozen solutions by sodium phosphates and citrates. Chem Pharm Bull. 2007;55:565–70.
33. Watanabe A, Morita S, Ozaki Y. Temperature-dependent structural changes in hydrogen bonds in microcrystalline cellulose studied by infrared and near-infrared spectroscopy with perturbation-correlation moving-window two-dimensional correlation analysis. Appl Spectrosc. 2006;60:611–8.
34. Yoshioka M, Hancock BC, Zografi G. Crystallization of indomethacin from the amorphous state below and above its glass transition temperature. J Pharm Sci. 1994;83:1700–5.

International Journal of Pharmaceutics 378 (2009) 167–176

Contents lists available at ScienceDirect

International Journal of Pharmaceutics

journal homepage: www.elsevier.com/locate/ijpharm

Pharmaceutical Nanotechnology

# Pharmaceutical quality evaluation of lipid emulsions containing $PGE_1$: Alteration in the number of large particles in infusion solutions

Hiroko Shibata *, Haruna Saito, Chikako Yomota, Toru Kawanishi

*National Institute of Health Sciences, Kamiyoga 1-18-1, Setagaya-ku, Tokyo 158-8501, Japan*

ARTICLE INFO

*Article history:*
Received 18 February 2009
Received in revised form 15 April 2009
Accepted 16 May 2009
Available online 22 May 2009

*Keywords:*
Emulsion
Prostaglandin $E_1$
Lipid particle
Release
Generics

ABSTRACT

There are two generics of a parenteral lipid emulsion of prostaglandin E1 ($PGE_1$) (Lipo-$PGE_1$) in addition to two innovators. It was reported the change from innovator to generic in clinical practice caused the slowing of drip rate and formation of aggregates in the infusion line. Thus, we investigated the difference of pharmaceutical quality in these Lipo-$PGE_1$ formulations. After mixing with some infusion solutions, the mean diameter and number of large particles were determined. Although the mean diameter did not change in any infusion solutions, the number of large particles (diameter >1.0 μm) dramatically increased in generics with Hartmann's solution pH 8 or Lactec® injection with 7% sodium bicarbonate. Next, we investigated the effect of these infusion solutions on the retention rate of $PGE_1$ in lipid particles. The retention rate of $PGE_1$ in these two infusion solutions decreased more quickly than that in normal saline. Nevertheless, there were no significant differences among the formulations tested. Our results suggest that there is no difference between innovators and generics except in mixing with these infusion solutions. Furthermore, that monitoring the number of large particles can be an effective means of evaluating pharmaceutical interactions and/or the stability of lipid emulsions.



## 1. Introduction

Prostaglandin E1 ($PGE_1$), which has a strong vasodilatory and antiplatelet activity, is clinically used to treat diseases such as periferal arterial occlusive diseases (Makita et al., 1997; Milio et al., 2003) and ductus arteriosus-dependent congenital heart disease (Kramer et al., 1995). However, $PGE_1$ has a very short half-life in blood and can elicit various side-effects (Golub et al., 1975; Schramek and Waldhauser, 1989). As a result, a lipid emulsion of $PGE_1$ (Lipo-$PGE_1$), in which lipid particles incorporating $PGE_1$ were coated with lecithin, was developed and applied for clinical treatment in Japan (Mizushima et al., 1983; Otomo et al., 1985). Because the lipid particles are efficiently distributed into the vascular lesion site, Lipo-$PGE_1$ accumulates in the lesion area and is therefore safer and more effective than free $PGE_1$ (Mizushima et al., 1990; Mizushima et al., 1983). Indeed, Lipo-$PGE_1$ is widely used to treat a number of conditions other than arterial occlusive diseases, such as cutaneous ulcer with diabetes and improvement of imaging ability for arterial portography. Two innovator formulations and two generic formulations have already been launched. The composition of each formulation is shown in Table 1. Although generic formulations contain olive oil instead of soybean oil, the other additives are the same as those found in the innovator formulations. Hydrochloric acid or sodium hydrate is added appropriately as a pH adjuster, and the pH of each formulation is adjusted 4.5–6.0.

Lipo-$PGE_1$ can be intravenously administered by bolus injection, or slowly administered as infusions by mixing with infusion solution. Recently, it was reported that the change from innovator to generic formulation in clinical practice caused the slowing of drip rate and formation of aggregates in the infusion line (Sakaya et al., 2005; Goto et al., 2005). This phenomenon was observed under alkaline conditions in the presence of calcium ions. The Lipo-$PGE_1$ has an approximate pH of 5. There are some cases where Lipo-$PGE_1$ is mixed into the infusion solutions of relatively high pH (e.g., Hartmann's solution pH 8; 7% sodium bicarbonate) in order to moderate vascular pain or venous inflammation. Furthermore, it has also been reported that generic formulations in saline solution exhibit lower retention rates of $PGE_1$ in lipid particles and weaker pharmacological activity in animal models than innovator formulations (Takenaga et al., 2007). Therefore, it is important to investigate the difference in pharmaceutical quality between innovator and generic formulations.

In the Japanese Pharmacopoeia, the diameter of lipid particles in a lipid emulsion is defined as being below 7 μm. Included in the tests for the preparation of a parenteral lipid emulsion is "Insoluble Particulate Matter Test for Injections" as well as "Test for Extractable Volume of Parenteral Preparations". The former test defines an examination by "Method 1. Light Obscuration Particle Count Test" or

* Corresponding author. Tel.: +81 3 3700 8486; fax: +81 3 3707 6950.
*E-mail address:* h-shibata@nihs.go.jp (H. Shibata).

0378-5173/$ – see front matter © 2009 Elsevier B.V. All rights reserved.
doi:10.1016/j.ijpharm.2009.05.026

**Table 1**
Formulas of Lipo-$PGE_1$.

| | Alprostadil (PGE1) | Purified soybean oil | Purified olive oil | Highly purified soybean lecithin | Oleic acid | Concentrated glycerin |
|---|---|---|---|---|---|---|
| Formulation #1 (innovator) | 5 μg | 100 mg | | 18 mg | 2.4 mg | 22.1 mg |
| Formulation #2 (innovator) | 5 μg | 100 mg | | 18 mg | 2.4 mg | 22.1 mg |
| Formulation #3 (generic) | 5 μg | | 100 mg | 18 mg | 2.4 mg | 22.1 mg |
| Formulation #4 (generic) | 5 μg | | 100 mg | 18 mg | 2.4 mg | 22.1 mg |

"Method 2. Microscopic Particle Count Test". Method 1 is preferably applied to injections and parenteral infusions. However, in cases where the preparation has a reduced clarity or increased viscosity, such as emulsions, colloids and liposomal preparations, the test should be carried our according to Method 2. The Pharmacopoeia of the United State of America (USP), ⟨788⟩ also defines a similar method for parenteral preparations. However, within recent years, ⟨729⟩ "Globule Size Distribution in Lipid Injectable Emulsions" is listed in the second supplement of USP30. This ⟨729⟩ provides two methods, "Method 1. Light-Scattering Method" for the mean diameter of lipid particles, and "Method 2. Measurement of Large Globule Content by Light Obscuration or Extinction method" for the extent of large-diameter particles (>5 μm), and is required to meet both criteria. This is based on the idea that the size of the lipid particles is critical because large-size fat globules can become trapped in the smallest of blood vessels such as capillaries with diameters between 4 and 9 μm (Guyton, 1991). The essential size characteristics of a lipid injectable emulsion include the mean diameter of lipid particles and the range of the various particle diameters distributed around the mean diameter (Driscoll et al., 2001). In this study, we investigated the formation of aggregates and measured the mean diameter and/or number of large-diameter particles. We also monitored $PGE_1$ retention rate in Lipo-$PGE_1$ to investigate the difference in the pharmaceutical quality of Lipo-$PGE_1$ formulations.

## 2. Materials and methods

### 2.1. Materials

Four Lipo-$PGE_1$ formulations as shown in Table 1 were used in this study. Palux® injection (Formulation #1, lot nos. O17H2 and I07H2, Taisho Pharmaceutical Co., Ltd., Tokyo, Japan), Liple® injection (Formulation #2, lot nos. P625J and P205H, Mitsubishi Tanabe Pharma Corporation, Osaka, Japan), Alyprost® injection (Formulation #3, lot nos. AB07A and AF07A, Nippon Chemiphar Co., Ltd., Tokyo, Japan), Prink® injection (Formulation #4, lot nos. 659109 and 659123, Taiyo Yakuhin Co., Ltd., Nagoya, Japan) were purchased from a drug seller in Japan. Otsuka normal saline, Aminofluid®, Lactec® injection and Meylon® (Otsuka Pharmaceutical Co., Ltd., Tokyo, Japan), Amicaliq® (Termo Corporation, Tokyo, Japan), Solita®-T No. 3 (Ajinomoto Co., Inc., Tokyo, Japan), Hartmann's Solution pH 8 and Nipro infusion set IS type (Nipro Pharma Corporation, Osaka, Japan), were purchased from a general sales agency for drugs in Japan. Lactec® injection with $NaHCO_3$ was composed of 500 ml Lactec® injection and 20 ml Meylon® (7% $NaHCO_3$ injection). The official $PGE_1$ reference standard was purchased from the Society of Japan Pharmacopoeia. Slide-A-Lyzer® Dialysis Cassette (molecular weight cutoff: 7 K, capacity: 0.1–0.5 ml) and Buoy used for dialysis method were purchased from Pierce (IL, US). Disposable syringes, 21- and 27-gauge needles were purchased from Terumo Corporation.

### 2.2. Particle size distribution analysis

A 2 ml aliquot of Lipo-$PGE_1$ was injected into a 500 ml infusion bag of different solutions. After mixing, the various solutions were incubated at room temperature. At the indicated time point, each mixed solution was collected and analyzed by measurement of dynamic light scattering or single particle optical sizing.

#### 2.2.1. Dynamic light scattering (DLS)

The particle size distribution and mean diameter of each Lipo-$PGE_1$ after mixing with different solutions were measured using a dynamic light scattering photometer DLS-7000 (Otsuka Electronics Co., Ltd., Osaka, Japan) equipped with a He–Ne laser source (wavelength, 632.8 nm). All DLS measurements were made with a scattering angle of 90°. Mixed solutions were diluted 15-fold with each infusion solution in order to obtain an appropriate scattering intensity. Data were gathered using a counting period of 100 s. Histogram analyses were performed to calculate the average particle size and standard deviation.

#### 2.2.2. Single particle optical sizing (SPOS)

An Accusizer 780A (Particle Sizing Systems, Santa Barbara, CA) was used to determine the number of large-diameter particles in the emulsions. This instrument is based on light extinction (LE) or light scattering (LS) that employs a single-particle optical sizing (SPOS) technique, and was equipped with an automatic dilution system. In this study, the summation mode, which is a combination of LE and LS, was applied to measure the number of particles >0.5 μm in diameter. Before commencing any measurements, the equipment was filled with each infusion solution by using the command "Start Vessel Flush". After ensuring the background count was below 100 counts/s, mixed solutions (about 5 ml) were injected into the sample chamber. Duplicate measurements were made for each sample at the appropriate time point using the following conditions; data collecting time, 60 s; flow rate, 60 ml/min; injection loop volume, 1.04 ml; syringe volume, 2.5 ml; second dilution factor, 40. We ascertained that this dilution factor maintained the per-milliliter counts below the coincidence limit for the sensor, thereby minimizing this source of error. The volume-weighted proportion of fat globules (PFAT) with a diameter of >5 μm ($PFAT_5$) was calculated by the command "Volume Fraction cal".

### 2.3. Zeta potential

Zeta potential was measured using a Zetasizer NanoZS (Malvern Instruments, Malvern, UK), which is based on laser Doppler velocimetry in an electric field. For each Lipo-$PGE_1$, 500 μl was diluted using 10 ml distilled water.

### 2.4. Determination of $PGE_1$ retention rate

#### 2.4.1. Assay for $PGE_1$

$PGE_1$ was measured by high-performance liquid chromatography (HPLC) using a post-column reaction. The HPLC system consisted of two constant pumps (LC-10ADvp, Shimadzu, Kyoto, Japan), a degasser (DGU-14A, Shimadzu), an automated pretreatment system, an autoinjector (SIL-10ADvp, Shimadzu), a UV/VIS detector (SPD-20AD, Shimadzu), a column oven (CTO-10ACvp, Shimadzu), and a system controller (SCL-10Asp, Shimadzu). $PGE_1$ was detected at 278 nm. The column used in this study was a 15 cm stainless-steel (4.6 mm i.d.) 5 μm Ø Mightysil ODS (Kanto Chem-